
[All ETDs from UAB](#)

[UAB Theses & Dissertations](#)

2021

Comprehensive Review And A Comparison Of Compliance Based Topology Optimization For Simply Supported Beams

Nicholas Yaw Asare Okai
University of Alabama at Birmingham

Follow this and additional works at: <https://digitalcommons.library.uab.edu/etd-collection>



Part of the [Engineering Commons](#)

Recommended Citation

Okai, Nicholas Yaw Asare, "Comprehensive Review And A Comparison Of Compliance Based Topology Optimization For Simply Supported Beams" (2021). *All ETDs from UAB*. 880.
<https://digitalcommons.library.uab.edu/etd-collection/880>

This content has been accepted for inclusion by an authorized administrator of the UAB Digital Commons, and is provided as a free open access item. All inquiries regarding this item or the UAB Digital Commons should be directed to the [UAB Libraries Office of Scholarly Communication](#).

COMPREHENSIVE REVIEW AND A COMPARISON OF
COMPLIANCE BASED TOPOLOGY OPTIMIZATION FOR
SIMPLY SUPPORTED BEAMS

by

NICHOLAS YAW ASARE OKAI

MUHAMMED M. SHERIF, COMMITTEE CHAIR
HAIBIN NING
NASSIM UDDIN
CHRISTOPER WALDRON

A THESIS

Submitted to graduate faculty of The University of Alabama at Birmingham,
in partial fulfillment of the requirements for the degree of
Master of Science

BIRMINGHAM, ALABAMA

2021

Copyright by
Nicholas Yaw Asare Okai
2021

COMPREHENSIVE REVIEW AND A COMPARISON OF COMPLIANCE BASED TOPOLOGY OPTIMIZATION FOR SIMPLY SUPPORTED BEAMS

NICHOLAS YAW ASARE OKAI

CIVIL ENGINEERING

ABSTRACT

Traditional structures consume large amounts of raw materials including cementitious composites and steel, which subsequently contribute to the increase in greenhouse gases. Furthermore, the recycling process of construction materials is challenging due to high cost and complex processes that involve crushing of concrete and melting of steel to the required composition. Therefore, it is necessary to optimize the materials used as well as the structural geometry to achieve maximum efficiency (i.e., demand/capacity) and decrease the carbon footprint of structures. The development of sustainable structures and eco-friendly infrastructures aims to minimize materials and energy consumption without impeding the overall performance. Also, an optimized design will lead to a reduction in the total construction cost. Over the past few decades, researchers have investigated the use of topology optimization to achieve the required strength of a component by optimizing its shape given a specific load.

Topology optimization is a mathematical method that seeks to optimize material layout within a specified design domain for a given set of boundary conditions and applied loads to achieve an efficient structure. Structural topology optimization can be classified into three categories including shape optimization, size optimization, and topology optimization. Size optimization usually deals with finding optimized cross-sectional

geometric properties of a member. Shape optimization seeks optimal shapes of a material domain without altering its topology; while topology optimization is an optimization technique that considers both size and shape in obtaining an optimal design. The methodologies for topology optimization include Solid Isotropic Material with Penalization (SIMP), and Evolutionary Topology Optimization (ETO). Both methodologies are based on the material distribution concept. In addition, the Level Set Method (LSM), is based on an implicit boundary description which is applied to track displacement and motions of the boundaries of a structure. Due to the computational requirements of topology optimization algorithms, it is usual to limit the optimization problem on a small structure that is subjected to a static load.

In this research, a comparison of the three topology optimization methodologies will be presented for simple problem of a simply supported beam subjected to a point load. Initially, a detailed review of the development, applications and formulation of the topology optimization methodology would be conducted. Then, the best values for the optimization parameters would be investigated and analyzed. Finally, three main compliance minimization optimization algorithms (SIMP, ESO and LSM) will be implemented and compared.

Keywords: topology optimization, compliance, SIMP, BESO, LSM

DEDICATION

To **YHWH**,

And the Aboagye Okai's family for their unconditional and immense love, support, and encouragement.

ACKNOWLEDGMENTS

First and foremost, I would like to express my sincere gratitude to my supervisor, Professor Muhammed Sherif, for his insightful comments, suggestions, and assistance at every stage of this research project.

I would also like extend my sincere thanks to Professor Nasim Uddin, Professor Christopher Waldron, and Professor Haibin Ning for serving as my master's committee members.

Most importantly, none of this could have been made possible without my family, who offered their encouragement, love and support through phone calls and messages every week-despite my own limited devotion to correspondence. Additionally, I want to thank my friends for the support during all the years I studied

TABLE OF CONTENTS

ABSTRACT.....	i
DEDICATION.....	iii
ACKNOWLEDGMENTS	iv
LIST OF TABLES.....	viii
LIST OF FIGURES	ix
LIST OF ABBREVIATIONS.....	xii
SYMBOLS.....	xiv
INTRODUCTION	1
1.1 Background	1
1.2 Objective	2
1.3 Organization of Thesis	3
LITERATURE REVIEW	4
2.1 History and Development of Topology Optimization.....	4
2.2 Applications of Topology Optimization	8
2.2.1 Macro-structural Applications	9

2.2.2	Micro-structural Applications.....	13
2.3.2	Objective Functions	16
2.3.3	Solid Isotropic Material/Microstructure with Penalization (SIMP).....	18
2.3.4	Evolutionary Topology Optimization (ETO).....	25
2.3.5	Level Set Method (LSM)	29
2.3.6	Numerical Instabilities	35
PROBLEM FORMULATION		39
NUMERICAL APPROACH		44
4.1	Solid Isotropic Material/Microstructure with Penalization (SIMP).....	44
4.2	Evolutionary Topology Optimization (ETO).....	46
4.2.1	Evolutionary Structural Optimization (ESO).....	46
4.2.2	Bi-Evolutionary Structural Optimization (BESO).....	47
4.2.3	Bilinear Interpolation	49
4.3	Level Set Method (LSM)	52
RESULTS AND DISCUSSION		58
5.1	Mesh Density Effect.....	58
5.2	Effect of Section Thickness.....	61
5.3	Effect of Penalization Factor.....	64
5.4	Effect of Desired Volume	66
5.5	Effect of Filter Radius	69
5.6	Effect of Element Rejection Ratio and Addition Ratio.....	70
5.7	Effect of Convergence Criteria	71

5.8	Effect of Radius of Nucleated Holes	72
5.9	Preferred Parameters in Optimization of Beams.....	72
CONCLUSIONS AND RECOMMENDATIONS		78
LIST OF REFERENCES		80

LIST OF TABLES

Table 1. Simulation Parameters for MBB Optimized using SIMP, BESO and LSM.....	42
Table 2. Preferred parameters for simulation	73
Table 3. Summary of Results from using Optimal Parameters for the Simulations.....	76

LIST OF FIGURES

Figure 1. Illustrations of a beam optimized using (a) size optimization, (b) shape optimization, and (c) topology optimization ^[3]	2
Figure 2. Schematic drawings of the designed Airbus A380 droop nose using topology optimization ^[10]	5
Figure 3. Structural models of TTO: (a) Ground structure ^[14] , (b) Transition of ground structure, and (c) final optimized structure	6
Figure 4. Types of topology optimization methodologies	8
Figure 5. Schematic drawings of the steering wheel of a Jaguar automobile: (a) initial design and (b) optimized design ^[37]	10
Figure 6. Topology optimization of a replacement to the femur bone ^[40]	11
Figure 7. Qatar National Convention Center Optimized for Architecture Design	12
Figure 8. Effect of Penalization Factor on the Effective Stiffness as a Function of Structural Density	20
Figure 9. Effect of Mesh Density on the (a) Minimum Compliance and (b) Time Required to Optimize a Structure ^[65]	21
Figure 10. Graphical Representation of a Level Set Function ^[79]	30
Figure 11. Various Types of Interpolation Functions: (a) Piecewise Linear Basis Function on 2D Domain Discretized by Triangles ^[77] , (b) Bi-Linear Basis Function on 2D Domain Discretized by Squares ^[77] , (c) Radial Basis Function Contour Plot ^[87] , and (d) Spectral Contour Plot ^[88]	33
Figure 12 Optimized beam with checkerboards	35
Figure 13. Illustration of the Messerschmidt-Bölkow-Blohm (MBB) model	40

Figure 14. Flowchart Representing the Procedure for SIMP.....	46
Figure 15. Flowchart Representing the BESO Algorithm Implemented.....	49
Figure 16. Nodal Classification Based on Its Location in a Structure.....	50
Figure 17. Effect of surface smoothing with an iso-line value of: (a) 0.1, (b) 0.5, (c) 0.7 and (d) 0.9 ^[95]	51
Figure 18. Illustration of the LSM procedure for solving a simple beam problem	57
Figure 19 Results plot for different number of discretized elements: (a) compliance (kNm), (b) displacement (mm), (c) volume fraction, (d) number of iterations of SIMP, BESO and LSM models	59
Figure 20 Plots of different mesh densities: (a), (b), and (c) represents 200×100 mesh densities of SIMP, BESO, and LSM, respectively. (d), (e), and (f) represents 200×75 mesh densities of SIMP, BESO, and LSM, respectively. (g), (h), and (i) represents 200×50 mesh densities of SIMP, BESO, and LSM, respectively. (j), (k), and (l) represents 150×50 mesh densities of SIMP, BESO, and LSM, respectively. (m), (n), and (o) represents 100×50 mesh densities of SIMP, BESO, and LSM, respectively.....	61
Figure 21 Results plot of section thickness: (a) compliance (kNm), (b) displacement (mm), (c) volume fraction, (d) number of iterations of SIMP, BESO and LSM models	62
Figure 22 Topology optimized beams with different thicknesses: (a), (b), and (c) are optimized beams with thickness of 20mm for SIMP, BESO, and LSM, respectively. (d), (e), and (f) are optimized beams with thickness of 40mm for SIMP, BESO, and LSM, respectively. (g), (h), (i), are optimized beams with thickness of 60mm for SIMP, BESO, and LSM, respectively	63
Figure 23 Results plot showing the effects penalization factor: (a) compliance (kNm), (b) displacement (mm), (c) volume fraction, and (d) number of iterations.....	64
Figure 24 Effect of penalization factor on beams: (a), (b), and (c) are penalization factor of 2 for SIMP, BESO, and LSM, respectively. (d), (e), and (f) are penalization factor of 4 for SIMP, BESO, and LSM, respectively. (g), (h), and (i) are penalization factor of 6 for SIMP, BESO, and LSM, respectively.....	66

Figure 25 Effectiveness of prescribed volume fraction: (a) compliance (kNm), (b) displacement (mm), (c) volume fraction, and (d) number of iterations.....	67
Figure 26 Optimized beams of different prescribed volume fractions: (a), (b), and (c) prescribed volume fraction of 0.5 for SIMP, BESO, and LSM, respectively. (d), (e), and (f) prescribed volume fraction of 0.6 for SIMP, BESO, and LSM, respectively. (g), (h), and (i) prescribed volume fraction of 0.7 for SIMP, BESO, and LSM, respectively. (j), (k), and (l) prescribed volume fraction of 0.75 for SIMP, BESO, and LSM, respectively. (m), (n), and (o) prescribed volume fraction of 0.8 for SIMP, BESO, and LSM, respectively. (p), (q) and (r) prescribed volume fraction of 0.9 for SIMP, BESO, and LSM, respectively	68
Figure 27 Effect of filter radius on topology optimized beams: (a) and (b) shows a filter radius of 1 for SIMP and BESO. (c) and (d) shows a filter radius of 1.5 for SIMP and BESO. (e) and (f) shows a filter radius of 2.....	70
Figure 28. Effect of removal and additional ratio on BESO optimized beams: (a) ER and ARmax 0.01, (b) ER 0.05 and ARmax 0.02, (c) ER and ARmax 0.05, (d) ER 0.1 and ARmax 0.02, (e) ER and ARmax 0.10, (f) ER 0.02 and ARmax 0.05, and (g) ER 0.02 and ARmax 0.10.....	71
Figure 29. Convergence limit check of topology optimized beams: (a) convergence criteria of 0.001, (b) convergence criteria of 0.0001, and (c) convergence criteria of 0.00001	71
Figure 30. Radius of nucleated holes: (a) 10% of No. of y-elements, (b) 20% of No. of y-elements, and (c) 50% of No. of y-elements	72
Figure 31. Optimized beams using preferred parameters: (a) SIMP, (b) BESO, and (c) LSM	73
Figure 32. Compliance plot of beams with preferred parameters: (a) compliance of SIMP, (b) compliance of BESO, (c) compliance of LSM.....	75
Figure 33. Displacement contour plot of optimized beams using preferred parameters: (a) displacement of SIMP, (b) displacement of BESO, (c) displacement of LSM, (d) displacement contour plot of SIMP, (e) displacement contour plot of BESO, (f) displacement contour plot of LSM	76
Figure 34. Volume Fraction Plot of Beams with Preferred Parameters Optimized with: (a) SIMP, (b) BESO, (c) LSM	77

LIST OF ABBREVIATIONS

AM	Additive Manufacturing
AR	Addition Ratio
BESO	Bi-Evolutionary Structural Optimization
CTO	Continuum Topology Optimization
ER	Evolution Rate
ERR	Element Rejection Ratio
ESO	Evolutionary Structural Optimization
ETO	Evolutionary Topology Optimization
FEA	Finite Element Analysis
FE	Finite Element
FEM	Finite Element Method
GTO	Gradient Topology Optimization
HCA	Hybrid Cellular Automat
LSF	Level Set Function
LSM	Level Set Method
MAD	Mandibular Advancement Devices
MMA	Method of Moving Asymptotes
MBB	Messerschmidt-Bölkow-Blohm
NGTO	Non-Gradient Topology Optimization
OC	Optimal Criteria

PDE	Partial Differential Equation
PLSM	Parametric Level Set Method
RBF	Radial Basis Function
RR	Rejection Ratio
SIMP	Solid Isotropic Material with Penalization
SLP	Sequential Linear programming
SQP	Sequential Quadratic Programming
TCTO	Truss Topology optimization
UCLD	Unconstrained Layer Damping

SYMBOLS

K_E	global stiffness
r_{min}	filter radius
x_e	element's density
x_{min}	minimum density (0 or 0.001)
α_i^e	Sensitivity of mean compliance
ρ_e	design variable
σ^{vm}	Von Mises stresses
σ_{xx}	x-x direction stress
σ_{yield}	Yield stress
σ_{yy}	y-y direction stress
$\nabla\phi$	Gradient of level set function
B	Gradient Matrix
C	Compliance
D	Nodal Displacement
D_e	Stress-Strain Matrix (constitutive matrix)
E	Elastic Modulus
ε	Strain
$g(x_e)$	Stress Limit
N	Shape Function/Number of Elements

P	Penalization Factor
U	Element's Displacement
V	Volume Fraction
Φ	Level Set Function
λ	Lagrange Multiplier
ν	Poisson's Ratio
σ	Stress
τ	Convergence Tolerance

CHAPTER 1

INTRODUCTION

1.1 Background

Structural topology optimization (STO) has been extensively explored and employed in various industries over the past few decades due to its ability in saving material and minimizing cost. STO can be classified into three main categories: 1) shape optimization, 2) size optimization, and 3) topology optimization. Shape optimization predicts the optimal shape or geometric features, while size optimization seeks the optimum structural cross-sectional area. Topology optimization seeks to achieve an optimized material layout with enhanced mechanical behavior in a specific design domain [1]. Eschenauer et al. presented a detailed overview of the history and applications of topology optimization [2]. Figures 1(a) to 1(c) illustrate the optimization of a beam using size, shape, and topology optimization, respectively [3].

Müller et al. compared the three methodologies of STO in optimizing truss structures [4]. Structures optimized with size optimization methodologies had the least weight. This was attributed to the restriction of material redistribution within each member of the structure. However, it was observed that size optimization requires a high computational time. Byun et al. implemented shape and topology optimization on high temperature superconductors taking into consideration the manufacturing limitations [5]. The results

indicated that the topology optimization method exhibited a high-performance in the layout design of superconductors.

In general, it is suggested to implement a simultaneous optimization method to achieve an optimized structure with high performance. At early stages, topology optimization could be performed solely to determine an efficient design concept. While, at later stages, size and shape optimization could be used to refine the design [6]. Furthermore, topology optimization is a preferred methodology for designing structures as it does not require an initial guess of the optimal shape or size [7].

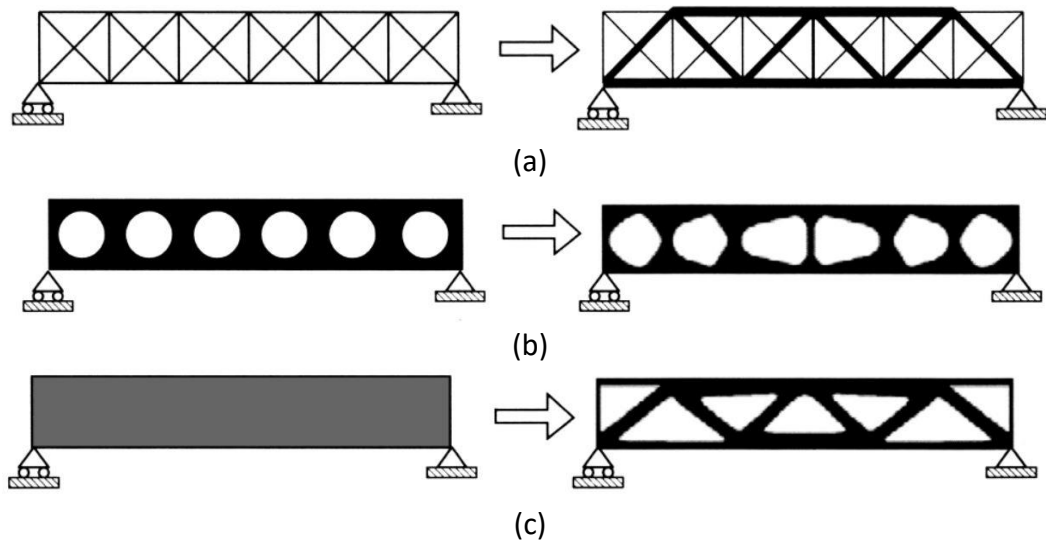


Figure 1. Illustrations of a beam optimized using (a) size optimization, (b) shape optimization, and (c) topology optimization^[3]

1.2 Objective

The concept and numerical methods surrounding topology optimization has evolved over the past decade. However, most research was conducted to develop new methodology to address certain limitations and numerical issues with a specific topology optimization

methodology. Therefore, there is a lack of literature and understanding in the differences between the various methodologies implemented and their performance. The goal of this research is to review and determine the optimal parameters for each optimization method. Furthermore, a comparison in the performance of three main compliance minimization topology optimization was conducted.

1.3 Organization of Thesis

The remainder of this thesis is organized as follows. Chapter 2 presents a literature review on topology optimization. The history, development, concept, and applications of topology optimization are discussed. A general finite element analysis (FEA) is also presented together with other mathematical and numerical formulations implemented in the general topology optimization. The latter part of the chapter discusses numerical instabilities normally encountered and its resolutions.

Chapter 3 provides details on the material properties and load assigned to a simply supported beam. The displacement for a conventional beam (un-optimized) was calculated and set as a benchmark for optimized beams. Parameters used for all simulations and the objective of the group of simulations is also discussed.

Chapter 4 focuses on the formulations and numerical implementation of the concepts discussed in chapter 2 for a simply supported beam with a point load mid-span.

In chapter 5, a comparative study of optimal parameters among the methodologies is presented. The optimal parameters were further used to optimize the simply supported beam with three methodologies of compliance minimization-based topology optimization.

Finally, chapter 6 presents the conclusions and recommendations.

CHAPTER 2

LITERATURE REVIEW

2.1 History and Development of Topology Optimization

In 1904, Michell investigated the analytical behavior of statically determined trusses and designed cost-efficient configurations by developing a methodology for structural topology optimization [8]. However, these configurations are not applicable for engineering practices due to its infinite number of elements [9]. In 1988, Bendsøe et al. enhanced the topology optimization algorithms for various structures [10]. This has led to the evolution of the topology optimization in a number of diverse fields such as civil, aerospace and mechanical engineering.

Figure 2 illustrates the schematic drawings of a drop nose rib of an Airbus A380 that has been designed using topology optimization [11]. Topology optimization is classified into three main categories: 1) continuum topology optimization (CTO), 2) truss topology optimization (TTO), and 3) truss-continuum topology optimization (TCTO) [12].

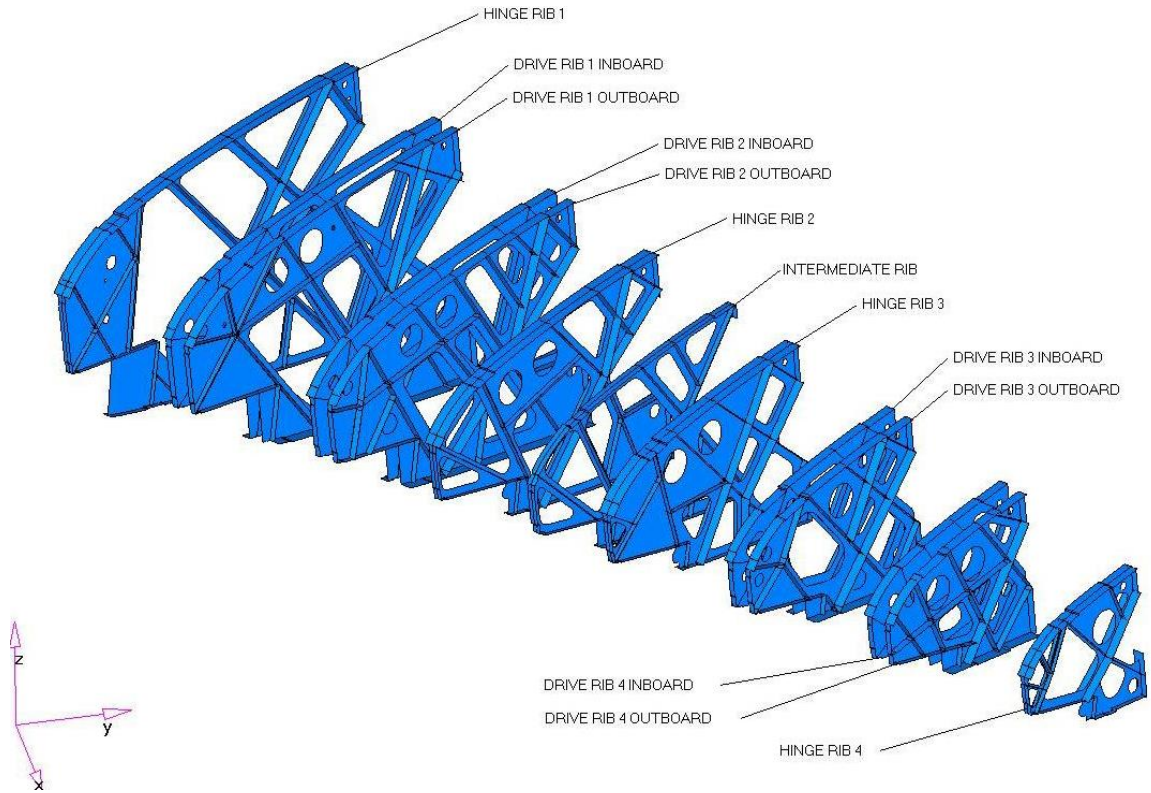


Figure 2. Schematic drawings of the designed Airbus A380 droop nose using topology optimization^[10]

In CTO, the structure is modeled as a solid continuum of different topology and a material interpolation scheme is implemented for isotropic material [13, 14]. The primary advantage of CTO is the ability of free form designability on a global stage [12]. On the other hand, TTO is a discrete optimization method. In discrete optimization methods the structure is modeled with discrete elements. The TTO employs the strut-and-tie model to develop a practical design for reinforced concrete structures [14]. Amir et al. investigated the use of TTO for placing reinforcement in concrete structures [15]. Furthermore, they extended the concept for the design of prestressed concrete [16]. Zhou et al. investigated

the methodology for optimizing deep beams [17]. In TTO, the initial structure (ground structure) is modeled with all candidate nodes and elements.

Figure 3(a) illustrates an example of a ground structure for a cantilever beam [14]. Depending on the implemented constraints, elements are removed from the ground structure to achieve the required objective functions.

Figure 3b and 3c illustrate the general transition of the ground structure, and the final optimized structure, respectively. However, the structure could be unstable if many elements are removed. Also, due to the dependency on the mesh size, the ground structure approach could be computationally expensive [14, 18, 19].

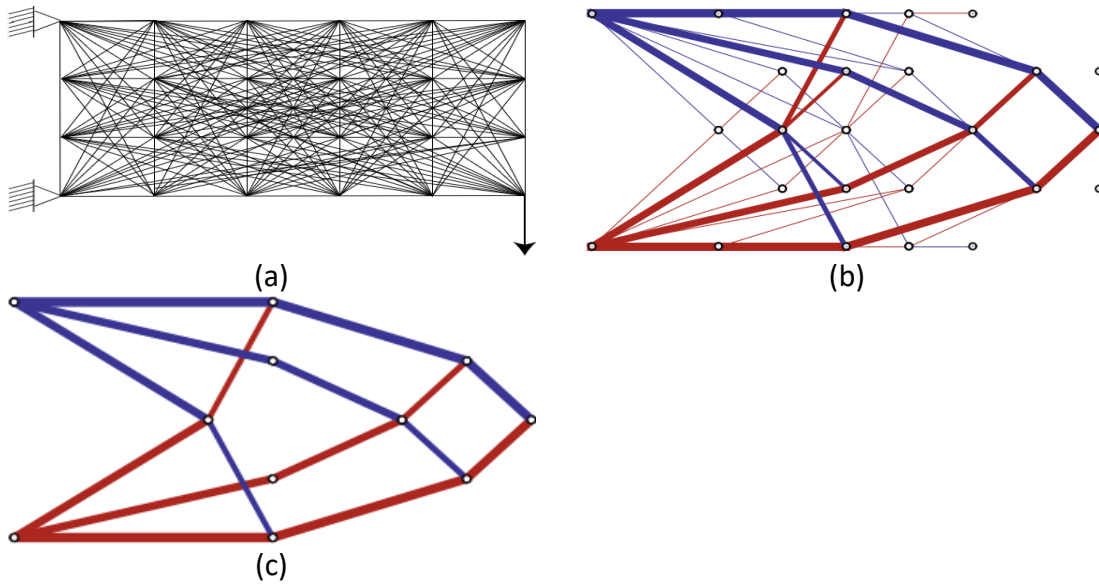


Figure 3. Structural models of TTO: (a) Ground structure^[14], (b) Transition of ground structure, and (c) final optimized structure

Smarslik et al. investigated the use of a hybrid TCTO by combining CTO and TTO to optimize a structure [20]. In the hybrid TCTO model, the CTO is used to consider the compressive strength. While the TTO is used to consider the tensile strength of the

concrete. Gaynor et al. implemented a hybrid bilinear TCTO to optimize a simply supported beam, a deep beam with a cutout, and a hammerhead pier [18]. Yang et al. extended the hybrid model of Gaynor et al.[21] to optimize three dimensional problems including: 1) a concrete block, 2) a pile cap, 3) a hammerhead pile, and 4) an anchorage zone of a prestressed beam [22]. In general, topology optimization approach can either be a gradient topology optimization (GTO) or a non-gradient topology optimization (NGTO). GTO utilizes both gradient of objective functions and constraint functions with respect to design variables (density) as opposed to NGTO which is gradient-free. Solid Isotropic Material/Microstructure with Penalization (SIMP), Evolutionary Topology Optimization (ETO) and Level-Set Method (LSM) are examples of GTOs. Examples of Non-gradient-based topology (NGTO) include phase-field methods, and topological derivatives [23, 24]. Figure 4 illustrates the various gradient and non-gradient topology optimization methods.

Wu et al. investigated a NGTO technique and suggested that the methodology performs better than SIMP that is a GTO methodology [25]. However, Andreassen et al. elaborated that NGTO methodologies do not necessarily converge to an optimum solution as they are using a global search [26]. Furthermore, for large structures NGTO techniques are time-consuming as the number of possible optimal solutions increase exponentially. Hare et al. compared GTO and NGTO techniques on structural engineering problems [27]. In general, the results suggest that GTP methodologies outperforms NGTO methodologies except for problems that a gradient method could not be defined.

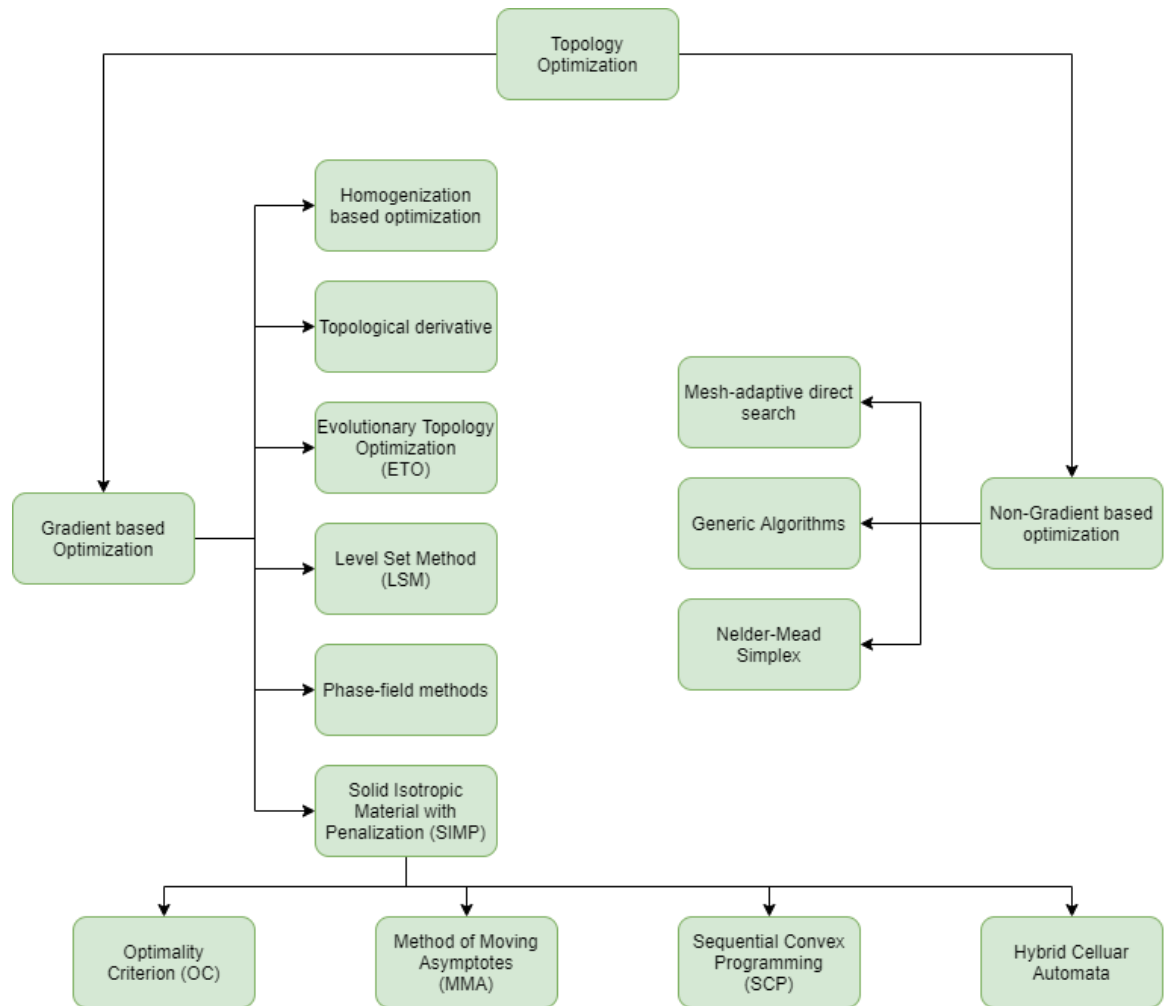


Figure 4. Types of topology optimization methodologies

2.2 Applications of Topology Optimization

In topology optimization, the material distribution, arrangement, and layout within a structure are imperative for high performance and optimality. Classical topology optimization seeks optimal distribution in an isotropic material within the design domain. The mechanical properties of a material are usually classified as isotropic, anisotropic, or orthotropic. The material composition could be classified as homogenous or

heterogeneous. Thus, there is a need to incorporate the material properties relative to the length scale. This would enable the models to replicate the actual behavior of structures. There are two classes of approach in the conceptual process of topology optimization namely macro-structural (geometry) and micro-structural (material). In general topology optimization is considered an early-stage design approach as the manufacturing constraints are not factored in the optimization procedure [28, 29].

2.2.1 Macro-structural Applications

The complexity of a structure can be significantly reduced by using homogenization methods to determine macroscopic material behavior. The basic concept of homogenization is to ‘smear-out’ microstructural behavior of periodic materials. Most structural topology optimization methods are implemented using basic elastic theories that are applicable at the macroscale. These methodologies assume that microscale dynamics are insignificant and could be ignored [30].

Topology optimization is significantly beneficial due to its production of lightweight structures and high mechanical performance systems. Nevertheless, it has a limited impact in real-life design problems due to the limitation of manufacturing complex shapes [7]. However, with the advancements in additive manufacturing (3D printing), researchers can experimentally investigate the performance of complex structures optimized using topology optimization. Gebisa et al. designed and experimentally investigated a 3D printed jet engine bracket using topology optimization algorithms [31]. Several researchers investigated the use of topology optimization for aerospace components that resist dynamic

loads and vibrations [32]. Munk et al. assessed the benefits of applying topology optimization in the structural design of aircraft components [7].

In the automotive industry, topology optimization has been implemented to achieve high-performing devices with the use of minimal materials [33-37]. The objective functions were to minimize mass while satisfying constraints in size and shape such as lower spokes radius, minimum casting thickness, symmetrical holes, and a lower casting area. Figures 5(a) and 5(b) display the initial and optimized design of a steering wheel for a Jaguar automobile [37]. Lee et al. designed a multicriteria optimized lightweight automotive parts based on a pareto-optimal to reduce noise, and vibrations [38]. Kim et al. implemented topology optimization by discretization of three-dimensional space for optimizing the suspension of a real vehicle [39].

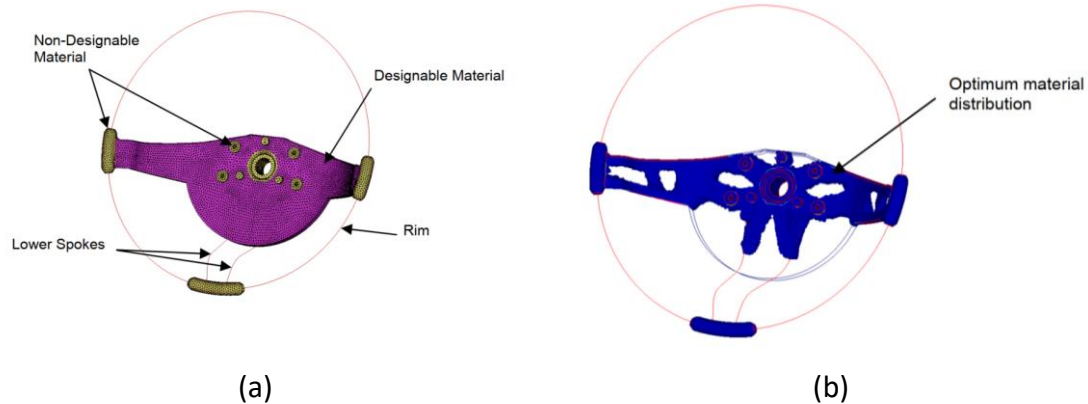


Figure 5. Schematic drawings of the steering wheel of a Jaguar automobile: (a) initial design and (b) optimized design^[37]

In biomedical engineering, topology optimization has been used for designing prosthetic devices to replace fractured bones [40]. Figure 6 illustrates the conventional topology optimization for a femur bone [40]. Park et al. designed a mandibular

advancement device (MADs) using topology optimization methodologies. The optimized devices exhibited lower and evenly distributed stress than the conventional devices [41]. The optimized devices revealed good compatibility with the patients surrounding bone tissue. Milazzo et al. implemented topology optimization to design middle ear prostheses [42]. Vilardell et al. investigated the manufacturing of topology optimized lightweight complex structures using laser power bed fusion (an additive manufacturing technique) [43].

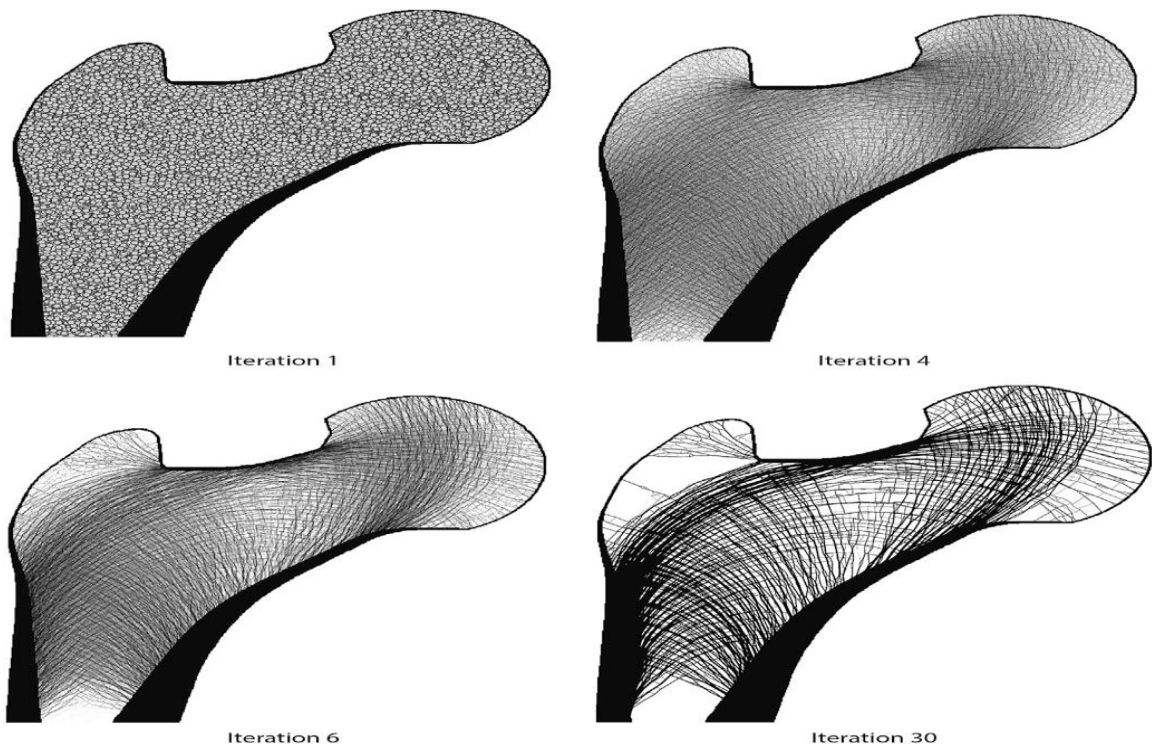


Figure 6. Topology optimization of a replacement to the femur bone^[40]

In civil engineering, structures can be optimized to have a better performance in resisting dynamic loads that may occur from earthquakes, tsunamis, and tornadoes. Furthermore, topology optimization enabled the design of efficient, low weight, and cost-

efficient structures. Beghenin et al. revised the connections of members through structural optimization of modern structures [44]. The optimized structure had complex shapes that minimized the materials needed and maintained the required stiffness. This would lead to a lower cost of construction. Huang et al. presented a topology optimized footbridge that has a span of 65 meters and is planned to be constructed in Australia [45]. Figure 7 illustrates a schematic diagram of an optimized conventional center in Qatar. Jewett conducted several numerical analysis and experimental work to ascertain the mechanical performance of topology optimized structures [46]. The results indicated that topology optimized structures outperformed conventional designs, specifically in the elastic range. It is worth noting that concrete structures are responsible for 5% of the global carbon emissions. Gan et al. illustrated that implementing topology optimization can reduce greenhouse gas emissions and contribute to the mitigation of the climate change phenomenon [47].



Figure 7. Qatar National Convention Center Optimized for Architecture Design

2.2.2 Micro-structural Applications

Microstructures are small scale structures that are composed of multiple base materials. The mechanical and electrical properties including the electrostatic forces, Brownian motion, and Van-der-Waals forces vary greatly from a micro-level to a macro-level [48]. It is worth noting that Allaire et al. indicated that the homogenization method could be implemented for materials with anisotropic behavior [49].

In 1995, Sigmund et al. implemented topology optimization on the microstructure of materials for tailoring the material properties (i.e., topology of material) by applying inverse of homogenization methodology [50]. Inverse homogenization involves the formulation of problem on a macroscopic level satisfying two conditions [51]. The first condition is that the homogenization problem formulated must be a tractable problem (i.e., it can be solved by a polynomial-time algorithm). The second condition is graded microstructures must be identifiable through the solution. Since then, topology complex mathematic problems that involves complicated geometric features, material properties and forces. In two-dimensional models, bilinear quadrilateral elements are used in the FEA. The global displacement (U) of a bilinear quadrilateral element can be approximated using Equation 1:

$$\begin{aligned}
 U &= N \times d & 1 \\
 \begin{Bmatrix} U(x, y) \\ V(x, y) \end{Bmatrix} &= \begin{bmatrix} N_1 & 0 & N_2 & 0 & N_3 & 0 & N_4 & 0 \\ 0 & N_1 & 0 & N_2 & 0 & N_3 & 0 & N_4 \end{bmatrix} \begin{Bmatrix} u_1 \\ v_1 \\ u_2 \\ v_2 \\ u_3 \\ v_3 \\ u_4 \\ v_4 \end{Bmatrix} & 2
 \end{aligned}$$

where $U(x,y)$ and $V(X,y)$ describe the global displacements at any point with coordinates (x_i, y_i) in an element. u_i and v_i are the local nodal displacements of an element. N_i represents the shape function. The strain (ε) of an element can also be calculated as given in Equation 3.

$$\varepsilon = \begin{Bmatrix} \varepsilon_x \\ \varepsilon_y \\ \gamma_{xy} \end{Bmatrix} = \begin{Bmatrix} \frac{\partial u}{\partial x} \\ \frac{\partial v}{\partial y} \\ \frac{\partial u}{\partial x} + \frac{\partial v}{\partial y} \end{Bmatrix} = B \times d \quad 3$$

where B represents the gradient matrix and d is the nodal displacements. B is computed in terms of the shape functions as given in Equation 4:

$$\begin{bmatrix} \frac{\partial N_1(x,y)}{\partial x} & 0 & \frac{\partial N_2(x,y)}{\partial x} & 0 & \frac{\partial N_3(x,y)}{\partial x} & 0 & \frac{\partial N_4(x,y)}{\partial x} & 0 \\ 0 & \frac{\partial N_1(x,y)}{\partial y} & 0 & \frac{\partial N_2(x,y)}{\partial y} & 0 & \frac{\partial N_3(x,y)}{\partial y} & 0 & \frac{\partial N_4(x,y)}{\partial y} \\ \frac{\partial N_1(x,y)}{\partial y} & \frac{\partial N_1(x,y)}{\partial x} & \frac{\partial N_2(x,y)}{\partial y} & \frac{\partial N_2(x,y)}{\partial x} & \frac{\partial N_3(x,y)}{\partial y} & \frac{\partial N_3(x,y)}{\partial x} & \frac{\partial N_4(x,y)}{\partial y} & \frac{\partial N_4(x,y)}{\partial x} \end{bmatrix} \quad 4$$

The stress-strain relationships of isotropic materials can either be plane-stress or plane-strain. For plane-stress conditions, the material constitutive matrix D_e can be represented by Equation 5:

$$D_e = \frac{E}{1 - \nu^2} \begin{bmatrix} 1 & \nu & 0 \\ \nu & 1 & 0 \\ 0 & 0 & \frac{1 - \nu}{2} \end{bmatrix} \quad 5$$

where E and ν represent the elastic modulus and Poisson ratio of the bilinear quadrilateral element, respectively. For plane-strain stress conditions, D_e the stress-strain matrix or constitutive matrix is calculated by Equation 6.

$$D_e = \frac{E}{(1 + \nu)(1 - 2\nu)} \begin{bmatrix} 1 - \nu & \nu & 0 \\ \nu & 1 - \nu & 0 \\ 0 & 0 & \frac{1 - 2\nu}{2} \end{bmatrix} \quad 6$$

The stress can be simplified as illustrated hereafter in Equation 7 and expanded based on the stress-strain relationship.

$$\sigma = D_e \times \varepsilon \quad 7$$

The element's global stiffness matrix can be calculated by equations 8 and 9:

$$K_E = \int_{V_e} B^T D_e B dv \quad 8$$

$$\begin{Bmatrix} f_{1x} \\ f_{1y} \\ f_{2x} \\ f_{2y} \\ f_{3x} \\ f_{3y} \\ f_{4x} \\ f_{4y} \end{Bmatrix} = \begin{bmatrix} k_{11} & k_{12} & \dots & k_{18} \\ k_{21} & k_{22} & \dots & k_{28} \\ \vdots & \vdots & \dots & \vdots \\ k_{51} & k_{52} & \dots & k_{58} \\ k_{61} & k_{62} & \dots & k_{68} \\ \vdots & \vdots & \dots & \vdots \\ k_{81} & k_{82} & \dots & k_{88} \end{bmatrix} \begin{Bmatrix} u_1 \\ v_1 \\ u_2 \\ v_2 \\ u_3 \\ v_3 \\ u_4 \\ v_4 \end{Bmatrix} \quad 9$$

where f_{ij} represents the nodal force with $i=(1,2,3,4)$ and $j=(x, y)$. From the generalized

Hooke's Law, a strain can be calculated using Equations 10 and 11:

$$\varepsilon = S \times \sigma \quad 10$$

$$\begin{bmatrix} \varepsilon_{xx} & \varepsilon_{xy} \\ \varepsilon_{yx} & \varepsilon_{yy} \end{bmatrix} = \begin{bmatrix} S_{11} & S_{12} \\ S_{21} & S_{22} \end{bmatrix} \times \begin{bmatrix} \sigma_{xx} & \sigma_{xy} \\ \sigma_{yx} & \sigma_{yy} \end{bmatrix} \quad 11$$

where S is the stiffness. The mean compliance can be calculated by Equation 12:

$$C = \frac{1}{S} \quad 12$$

The mean compliance can also be defined as the strain energy (compliance) and computed

using Equations 13 and 14:

$$U_c = \frac{1}{2} \iiint_V \{\varepsilon\}^T \{\sigma\} dV \quad 13$$

$$U_c = \frac{1}{2} \iiint_V \{\varepsilon\}^T [D_e] \{\varepsilon\} dV \quad 14$$

The global stiffness matrix of the whole structure can be assembled by Equation 15:

$$[K] = \sum_{E=1}^N [K_E] \quad 15$$

The force and displacement on the structure are, therefore, computed using Equation 16:

$$\{F\} = [K]\{d\} \quad 16$$

2.3.2 Objective Functions

In optimization problems, an objective should be set for the numerical algorithms to solve and find an optimal solution. In the structural domain, the most common objective functions are minimization of compliance (i.e., minimization of strain energy) and stress-based objective functions. Stress-based objective functions relate the applied stress to the yielding stress of the structural members.

2.3.2.1 Compliance Minimization Problems

In compliance minimization problems, the objective function is to minimize strains while maximizing the stiffness of a structure. In this formulation, the volume is a constraint and set to the desired amount of material to be used. The objective function can be formulated as given in Equation 17:

$$\min(x) : C(x) = U^T K U \quad 17$$

subjected to a constraint of the desired volume in Equations 18 to 19:

$$\sum_{e=1}^N \rho_e \leq V_o \quad 18$$

$$0 < \rho_{min} \leq \rho_e \leq 1 \quad 19$$

where C represents compliance, ρ_e is the design variable (density) of an element and V_o is the volume constraint. The ρ_{min} is a minimum density assigned voids to avoid non-singularity and is often set as 0.001.

2.3.2.2 Stress Based Problems

In a practical approach, structural members are designed with high performance (i.e., each structural member should be optimized to the applied stress to lower construction cost). In stress-based problems, the structure is optimized in reference to the ratio of the

applied forces to each element's strength. The most common failure criterion that is used in stress-based problems is the Von-Mises yield stress. In stress-based problems, the objective function is to minimize the volume of the material used while subjected to a stress constraint. The objective function can be formulated as elaborated in Equations 20 to 22:

$$\min(x) \quad V = \sum_{e=1}^N \rho_e \quad 20$$

subjected to a constraint of the stress limit:

$$g(x_e) = \frac{\sigma^{vm}}{\sigma_{yield}} < 1 \quad 21$$

$$0 < \rho_{min} \leq \rho_e \leq 1 \quad 22$$

where V is the structural volume minimized, ρ_e is the design variable, σ^{vm} is the Von Mises stress in the element, and σ_{yield} is the yield stress of the material. An element's material is retained in the design domain provided that the constraint function is satisfied.

The Von-Mises failure criterion is given by Equation 23:

$$\sigma^{vm} = \sqrt{\sigma_{xx}^2 + \sigma_{yy}^2 - \sigma_{xx}\sigma_{yy} + 3\tau_{xy}^2} \quad 23$$

where σ_{xx} represents the stresses along the x - x direction, σ_{yy} is the stresses along the y - y direction, and τ_{xy} is the shear-stress in the x - y direction. Beyond the yield stress the element's material would fail.

However, the constraint function defined by Equation 21, can cause stress singularities (i.e., a phenomenon of abnormalities due to infinite level of stresses). The stress singularities occur for elements with very low densities (i.e., near zero). To overcome this issue, Duysinx et al. introduced a stress relaxation technique [57]. This was inspired by the research work conducted by Cheng et al. [58]. The constraint function is redefined in Equations 24 and 25:

$$\rho_e \left(\frac{\sigma^{vm}}{\rho_e^P \sigma_{yield}} - 1 \right) \leq \epsilon - \epsilon \rho_e \quad 24$$

$$\epsilon \leq \rho_e \leq 1 \quad 25$$

where ϵ , is a relaxation parameter and is greater than zero, P is a penalization exponential value greater than 1 is recommended. Also, an effective material modulus can be used to handle the stress singularities. The effective homogenized modulus (E^e) can be defined as given in Equation 26:

$$E^e = \rho_e^P E_o \quad 26$$

where E_o is the elastic modulus of solids. The macroscopic stress based on the effective modulus can be calculated using Equation 27:

$$\sigma^e = D_e E^e \epsilon_e \quad 27$$

To properly account for intermediate densities, the microscopic stress should be defined in-term of the macroscopic stress as given in Equation 28. It is worth noting that the penalization factor is used to preserve the stress behavior to account for material porosity [59].

$$\sigma(x) = \frac{\sigma^e}{\rho_e^P} = \frac{D_e E^e \epsilon_e}{\rho_e^P} \quad 28$$

2.3.3 Solid Isotropic Material/Microstructure with Penalization (SIMP)

Solid Isotropic Material/Microstructure with Penalization (SIMP) is the most popular topology optimization method. SIMP implements a material density distribution approach that is based on the homogenization method. The homogenization method models the material composition with infinite microscopic voids within a design domain. The method eliminates the micro-portion of an element that has poor performance, rather than eliminating the whole element [10, 60]. However, the homogenization method is not widely used due to the fact that real structural applications consist of elements that are solid

or void in a specific design domain. In order to overcome this limitation, the SIMP was developed to optimize structures with porous properties [49]. Furthermore, SIMP could be used to define anisotropic materials [48, 49].

In SIMP, the structure's volume is discretized into a grid of elements (isotropic solid microstructures) with each having a fractional density of the material. The structure can develop any density between 0 and 1. A lower bound (minimum density) closer to zero is selected to ensure stability in the formulation and prevention of singularity in the finite element analysis (FEA). Furthermore, elements with partial density are penalized. The penalization factor is an exponential parameter applied to significantly reduce the stiffness of elements with small partial densities as they are insignificant in resisting loads [61].

Bendsøe et al. investigated and compared different approaches in relation to material interpolation scheme with the ability to produce densities varying from 0 to 1 [62]. A non-linear interpolation scheme achieved the best optimized structures. The material elastic modulus and stress could be formulated using Equations 29 and 30, respectively:

$$E(\rho) = \rho^P E_0 \quad 29$$

$$\sigma^Y(\rho) = \rho^P \sigma_0^Y \quad 30$$

where $E(\rho)$ is the effective elastic modulus, ρ is the design variable, P is a penalization power usually > 1 , E_0 is the overall elastic modulus, $\sigma^Y(\rho)$ is the effective yield stress, and σ_0^Y is the overall yield stress.

Figure 8 illustrates the effect of penalization factor on relative stiffness in terms of the material density. In 2005, Bruns et al. developed a SINH method (SINH is neither an acronym nor affiliated to a hyperbolic function) [63]. They reevaluated the SIMP method with filtering and alternative formulation for solid-void topology optimization.

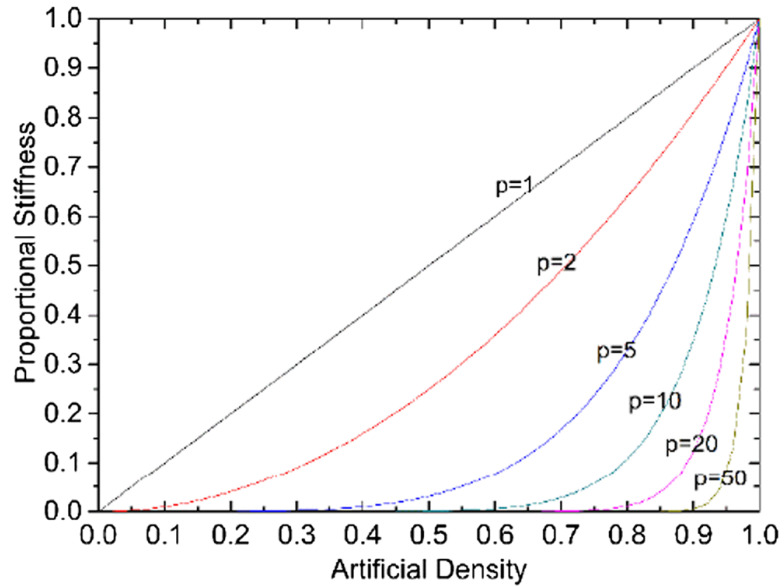


Figure 8. Effect of Penalization Factor on the Effective Stiffness as a Function of Structural Density

To measure the performance of a structures and determine the new design variable for the next iteration, sensitivity analysis is implemented. Sensitivity analysis is the derivative of the objective function with respect to the design variable. There are several approaches for implementing sensitivity analysis including but not limited to: 1) optimal criteria (OC), 2) method of moving asymptotes (MMA), 3) sequential linear programming (SLP), 4) sequential quadratic programming (SQP), and 5) hybrid cellular automat (HCA) [64]. Fanni et al. compared the sensitivity analysis methods on optimizing structures with various meshing density and an objective function of minimizing compliance [65]. The results indicated that OC and MMA are the most efficient due to their computation cost and optimal structural results.

Figure 9(a) and 9(b) illustrate the effect of the meshing density on the minimum compliance and number of iterations required [65].

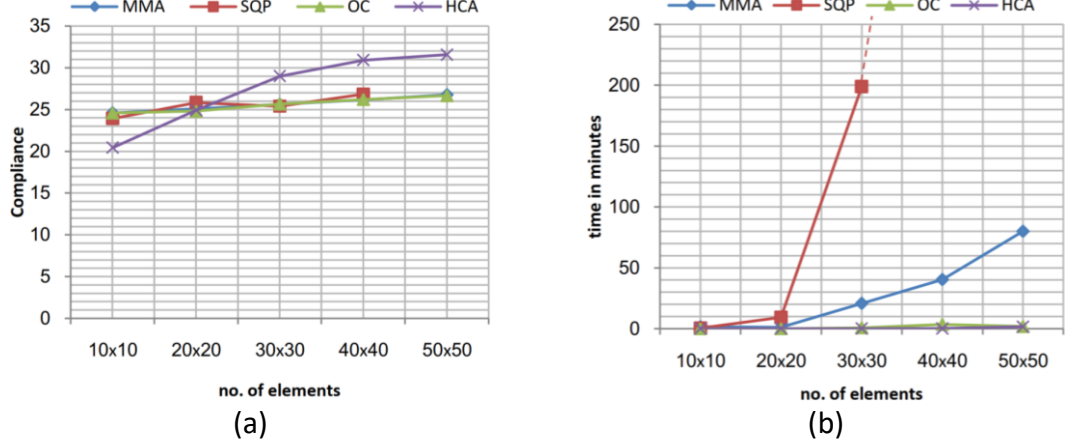


Figure 9. Effect of Mesh Density on the (a) Minimum Compliance and (b) Time Required to Optimize a Structure^[65]

2.3.3.1 Optimal Criteria (OC)

The optimal criteria method is a classical approach for solving topology optimization method especially for compliance-based problems due to its efficiency. OC method is used in updating the design variables (densities) in the structure. The heuristic scheme for updating design variables is computed using Equation 31.

$$\begin{aligned}
 & \text{if } x_e \beta_e^\eta \leq \max(x_{min}, x_e - m) \\
 & \quad x_e^{new} = \max(x_{min}, x_e - m) \\
 & \text{if } \max(x_{min}, x_e - m) < x_e \beta_e^\eta \leq \min(1, x_e + m) \\
 & \quad x_e^{new} = x_e \beta_e^\eta \\
 & \text{if } \min(1, x_e + m) < x_e \beta_e^\eta \\
 & \quad x_e^{new} = \min(1, x_e + m)
 \end{aligned} \tag{31}$$

where m is defined as a positive move limit (usually assigned as 0.2), η is a numerical damping coefficient which can be from zero to one (usually assigned as 0.5) to ensure stability of the iterations [66, 67]. β_e is computed based on the objective function and constraint function from an optimality condition as defined in Equations 32 and 33 for compliance and stress-based problems, respectively.

$$\beta_e = \frac{-\frac{\partial c}{\partial x_e}}{\lambda \frac{\partial V}{\partial x_e}} \quad 32$$

$$\beta_e = \frac{\frac{\partial v}{\partial x_e}}{\lambda \frac{\partial g}{\partial x_e}} \quad 33$$

where λ is a global Lagrangian multiplier obtaining through an iterative process by a bisectioning algorithm. In the case of the compliance-based, the objective function is compliance minimization subjected to a volume constraint. While in the stress-based the objective function is volume minimization subjected to a stress constraint. ∂c and ∂g are the sensitivity of the objective functions (derivative of the objective functions) and are calculated by Equations 34 and 35, respectively:

$$\frac{\partial c}{\partial x_e} = -p(x_e)^{p-1} u_e^T k_0 u_e \quad 34$$

$$\frac{\partial v}{\partial x_e} = v_e \quad 35$$

where p is the penalization factor (usually ≥ 3) and $\frac{\partial g}{\partial x_e}$ is the derivative of stress-constraint

with respect to the design variable, calculated by Equation 36:

$$\frac{\partial g}{\partial x_e} = \frac{\partial(\rho_e^{p-q}) D_o B_e u_e}{\partial x_e \sigma_{yield}} + \frac{\rho_e^{p-q} D_o B_e \partial u_e}{\sigma_{yield} \partial x_e} \quad 36$$

the right part of the derivate ($\frac{\partial u_e}{\partial x_e}$) can be solved using the adjoint method as defined in

Equations 37 to 40 which represent an efficient way to evaluate the gradient of the constraint.

$$\frac{\partial(KU)}{\partial x_e} = \frac{\partial F}{\partial x_e} \quad 37$$

$$\frac{\partial K}{\partial x_e} U + K \frac{\partial U}{\partial x_e} = \frac{\partial F}{\partial x_e} \quad 38$$

$$K \frac{\partial U}{\partial x_e} = \frac{\partial F}{\partial x_e} - \frac{\partial K}{\partial x_e} U \quad 39$$

$$\frac{\partial U}{\partial x_e} = K^{-1} \left(\frac{\partial F}{\partial x_e} - \frac{\partial K}{\partial x_e} U \right) \quad 40$$

however, $\frac{\partial F}{\partial x_e}$ is 0 since the applied force is not dependent on the design variable (density),

then the Equation 40 can be reduced to Equation 41.

$$\frac{\partial U}{\partial x_e} = -K^{-1} \left(\frac{\partial K}{\partial x_e} U \right) \quad 41$$

The homogenized stiffness could then be computed by Equation 42:

$$\frac{\partial K}{\partial \rho_e} = P x_e^{P-1} k_e^0 \quad 42$$

where f_0 is the function of density. Thus, the derivative of macroscopic stiffness is

computed by Equation 44:

$$\frac{\partial u}{\partial x_e} = -K^{-1} (P x_e^{P-1} k_e^0) U \quad 43$$

$$\frac{\partial u}{\partial x_e} = -K^{-1} (P x_e^{P-1} k_e^0) U \quad 44$$

Therefore,

$$\frac{\partial g(\rho_{x_e})}{\partial x_e} = \frac{(P - q) \rho_e^{P-q-1} D_o B_e u_e}{\sigma_{yield}} + \frac{\rho_e^{P-q} D_o B_e}{\sigma_{yield}} \left[- (x_e^P k_e^0)^{-1} (P x_e^{P-1} k_e^0) U \right] \quad 45$$

The OC method might be easier to implement, nonetheless, it has some deficiencies.

The OC method is a non-general optimization method and has encountered converge issues for most constraints other than compliance. It also suffers from a couple of numerical instabilities and cannot handle problems with constraints that exceed the applied constraints [65].

2.3.3.2 Moving Method Asymptotes (MMA)

In 1987, The MMA developed by Svanberg [68]. It is a non-linear programming technique based on a special convex approximation. The MMA methodology can handle general non-linear optimization problems with a denser mesh, and large number of design

variables. This is applicable given that the derivatives of the constraint functions with respect to the design variables can be analytically or numerically solved. The general minimization problem can be formulated based on Equations 46 to 49:

$$f_0(x) \quad 46$$

subjected to

$$f_i(x) \leq \hat{f}_i \quad 47$$

for $i=1, \dots, m$ and where m is the number of constraints for the constraint function, and

$$x_{lj} \leq x_j \leq x_{uj} \quad 48$$

for $j=1, \dots, n$ and n is the number of design variables for a lower bound (x_{lj}) and upper

bound (x_{uj}) of the design variable. MMA uses a sub-problem concept where a sub-problem $P^{(k)}$ is generated by substituting the constraint function with P through an explicit approximating function $f_i^{(k)}$. $f_i^{(k)}$ is derived through a first order Taylor expansion in a reciprocal elemental size ($1/x_j$). $f_i^{(k)}$ is defined for a range of lower and upper moving asymptotes chosen for the number of variables as seen in Equation 49:

$$L_j^{(k)} < x_j^{(k)} < U_j^{(k)} \quad 49$$

where $j=1, \dots, n$. The lower and upper moving asymptotes variables assist in achieving

convergence during the iterative process. Also, the moving asymptotes stabilizes the oscillational behavior in the structure. $f_i^{(k)}$ is formulated as given in Equation 50:

$$f_i^{(k)}(x) = r_i^{(k)} + \sum_{j=1}^n \left(\frac{P_{ij}^{(k)}}{U_j^{(k)} - x_j} + \frac{q_{ij}^{(k)}}{x_j - L_j^{(k)}} \right) \quad 50$$

where

$$P_{ij}^{(k)} = \begin{cases} (U_j^{(k)} - x_j^{(k)})^2 \frac{\partial f_i}{\partial x_j}, & \text{if } \frac{\partial f_i}{\partial x_j} > 0 \\ 0, & \text{if } \frac{\partial f_i}{\partial x_j} \leq 0 \end{cases} \quad 51$$

$$q_{ij}^k = \begin{cases} 0, & \text{if } \frac{\partial f_i}{\partial x_j} \geq 0 \\ -(x_j^{(k)} - L_j^{(k)})^2 \frac{\partial f_i}{\partial x_j}, & \text{if } \frac{\partial f_i}{\partial x_j} < 0 \end{cases} \quad 52$$

$$r_i^{(k)} = f_i(x^{(k)}) - \sum_{j=1}^n \left(\frac{P_{ij}^{(k)}}{U_j^{(k)} - x_j} + \frac{q_{ij}^{(k)}}{x_j - L_j^{(k)}} \right) \quad 53$$

2.3.4 Evolutionary Topology Optimization (ETO)

There are two main methodologies of evolutionary topology optimization (ETO) including: 1) evolutionary structural optimization (ESO) and 2) Bi-evolutionary structural optimization (BESO).

2.3.4.1 Evolutionary Structural Optimization (ESO)

In 1992, the Evolutionary structural optimization (ESO) was first proposed by Xie et al [69]. It has been continuously developed over the last three decades in solving optimization problems. ESO is also known as a “hard-kill” method. In a hard kill method, discretized elements are assigned a density value of either one (solid) or zero (void) with no intermediate densities [61]. The general concept of ESO is the gradual removal of incompetent materials in a design domain [45]. The initial application of ESO was in relation to stresses in a design domain to retain elements with significant “stress capacity” [70].

In a stress-based problem, ESO removes elements with a stress value less than a prescribed stress limit after each optimization iteration. The stress limit is imposed using a rejection ratio based on a failure criterion such as the Von-Mises Stress [71]. The elimination process

removes elements with insignificant stress performance [45]. The formulae used for the removal of elements is given in Equation 54:

$$\frac{\sigma_e^{vm}}{\sigma_{max}^{vm}} < RR_i \quad 54$$

The optimization iteration continues up to reaching a steady state. At steady state, no elements are further eliminated. The evolution ratio (ER) is used to update the rejection ratio at the end of each i^{th} iteration. This is given by Equation 55:

$$RR_{i+1} = RR_i + ER \quad 55$$

On the contrary, in compliance minimization problems, the total strain energy is computed by using Equation 56:

$$C = \frac{1}{2} F^T u \quad 56$$

where $\{F\}$ is the nodal forces, and $\{u\}$ is the displacement forces. It is possible to derive the change in compliance of a structure using Equation 57:

$$\Delta K = K^e - K = -K_i \quad 57$$

where K^e is the effective stiffness of the structure after the elements are removed and K_i is stiffness of the i^{th} element that is removed at the current iteration. Since, the eliminated elements are assumed to have insignificant impact on the load applied thus the change in displacement can be computed using Equations 58 to 60:

$$u = K^{-1} F \quad 58$$

$$u = K^{-1} K u \quad 59$$

$$\Delta u = -K^{-1} \Delta K u \quad 60$$

Therefore, the change in compliance can be computed by Equations 61 to 63:

$$\Delta C = \frac{1}{2} F^T \Delta u \quad 61$$

$$\Delta C = -\frac{1}{2} F^T K^{-1} \Delta K u \quad 62$$

$$\Delta C = \frac{1}{2} u_i^T K_i u_i \quad 63$$

where u_i is the displacement of the i^{th} element. Hence, the sensitivity number for the mean compliance is defined by Equation 64:

$$\alpha_i^e = \Delta C = \frac{1}{2} u_i^T K_i u_i \quad 64$$

Chu et al. determined that the sensitivity is the most effective criterion for removing elements and to find an optimal design with the minimum compliance [70].

2.3.4.2 Bi-Evolutionary Structural Optimization (BESO)

The BESO is capable of simultaneously adding and removing elements in each iterative stage. In 1996, Papadrakakis et al. introduced this concept of both additional and removal of elements [72]. Nonetheless, Querin et al. were the first to systematically explore it [73]. An additional ratio (AR) is introduced in BESO. The additional ratio re-introduces elements removed previously due to low sensitivity but are currently exhibiting high sensitivity even as voids. A simple compliance minimization problem can generally be defined by Equation 65:

$$C = \frac{1}{2} F^T u \quad 65$$

subjected to a volume constraint given by Equation 66:

$$\sum_{i=1}^N V_i X_i = V^d \quad 66$$

where V_i is the element's volume, X_i is the design variable, and V^d is the desired volume fraction. The volume constraint was introduced in BESO due to convergence issues in ESO. Therefore, the sensitivity of each element can be computed by Equation 67:

$$\alpha_i^e = \Delta C = \frac{1}{2} u_i^T K_i u_i \quad 67$$

However, for a problem with a non-uniform mesh, the sensitivity number can be computed using Equation 68:

$$\alpha_i^e = e_i = \frac{\left(\frac{1}{2} u_i^T K_i u\right)}{V_i} \quad 68$$

2.3.4.3 Element's Removal and Addition Criteria

The initial stage in the ESO and BESO algorithm is to specify a desired volume ratio (V^D). The volume fraction of the optimized structure in the next iteration (i.e., k+1) by provided in Equation 69:

$$V_{k+1} = \begin{cases} V_k(1 + ER), & \text{if } V_k < V^D \\ V_k(1 - ER), & \text{if } V_k > V^D \end{cases} \quad 69$$

where ER is the evolution ratio, with a sensitivity threshold is set based on the ER. While the addition ratio (AR) is used to define the percentage of voids with high sensitivity to be filled. The elements added should consist of a sensitivity value above the sensitivity threshold. However, the elements added are subjected to a maximum percentage of elements to be added (AR_{max}). This process is repeated until the convergence criteria is met as defined by Equation 70:

$$\frac{|\sum_{i=1}^N C_{k-i+1} - \sum_{i=1}^N C_{k-N-i+1}|}{\sum_{i=1}^N C_{k-i+1}} \leq \tau \quad 70$$

where N is the number of iterations to be considered for computing the mean compliance of N iterations, and τ is the convergence tolerance [45].

2.3.5 Level Set Method (LSM)

In 1988, Osher et al. introduced the level set methodology to model surfaces with moving curvatures [74]. In 1998, Haber et al. implemented the level set methodology for topology optimization [75]. The level set method (LSM) is an implicit boundary description method which defines material phase interfaces by a level set function (LSF) [76, 77]. LSM is an efficient way to represent and track the evolution of interfaces and surfaces. Contrary to explicit boundary description (e.g., splined-based), implicit boundary description has the capabilities to handle topological changes [77, 78]. The structure's volume is represented by a Level Set Function (LSF). This is done by means of an auxiliary continuous function (ϕ) that consists of a number of variables which represent the number of spatial dimensions [76]. The Level Set Function (LSF) consists of the material interface (Γ), material domain (Ω), and void domain (D/Ω). It represents a closed curve that can be defined as given in Equation 71:

$$\Gamma = \{(x, y, z) | \phi(x, y, z) = 0\} \quad 71$$

Γ is represented as a zero-level set by the function and x , y , and z respecting its coordinates. Figure 10 is a graphical representation of a level set function [79]. The function ϕ is negative when outside the region delimited by the curve or surface and positive when inside the region as seen.

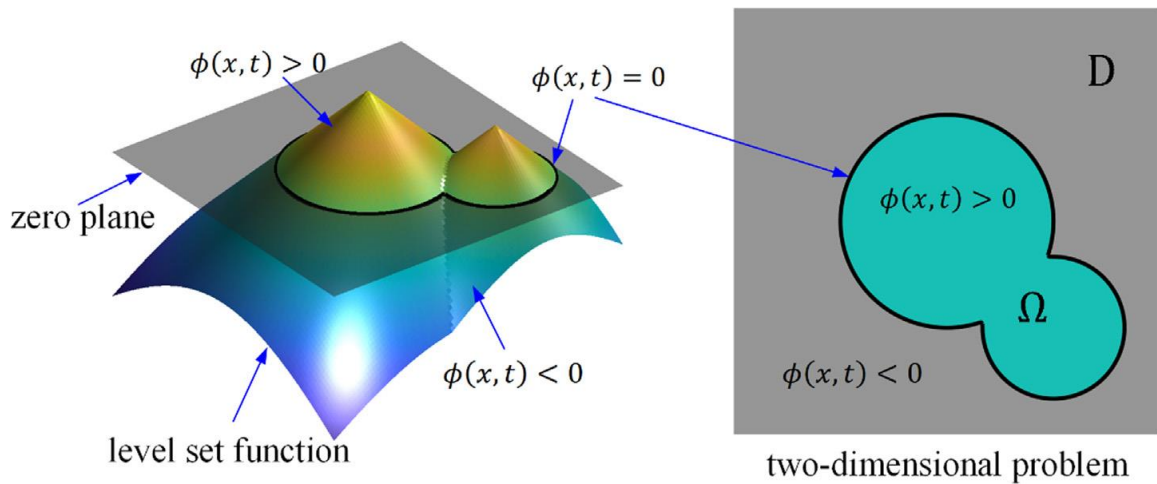


Figure 10. Graphical Representation of a Level Set Function^[79]

LSM utilizes the Eulerian approach. The Eulerian approach can perform numerical computations without parameterization. It has exhibited high performances in solving problems having complex surfaces and surface mesh extractions [80]. The implementation of partial differential equation (PDE) in the Eulerian approach assists in defining other property parameters such as velocity, temperature, and pressure with respect to time and space.

Nonetheless, Fu et al. presented an effective parametric level set method (PLSM) [81]. The approach was developed for macro-periodic structures with sub-structuring such that a condensing linear system is to be solved. The parametric level set approach is an extension of the conventional LSM. PLSM is superior as there is no need for re-initialization. This leads to numerical robustness and efficiency [82]. Due to its computational efficiency, LSM has been widely implemented during the past decade.

Jiang et al. proposed a new parametric level set scheme for structural topology optimization [82]. They constructed a cardinal basis function based on the radial basis function (RBF).

The essence of applying cardinal basis function is to precisely specify the range of design variables. Delgado et al. optimized three-dimensional fully viscoelastic structures and two-dimensional unconstrained layer damping (UCLD) using LSM [83]. Chen et al. presented a novel level set-based method using scanning path-optimization that enabled the development of a well-defined geometric parts [84]. This was accomplished by a layer-wise continuous scanning of path-optimization.

2.3.5.1 Parameterization

A curve could be represented by a one-dimensional equation with other parameters that define the shape and its behavior. This is known as parameterization. The parameterization is used to define the details of the LSF and the nature of the optimization problem (i.e., nonlinearity and monotonicity) [77]. LSF parameterization can be distinguished by 1) support size of basis functions, 2) type of interpolation scheme, and 3) shape of basis function.

The support size of a basis function defines the regions within a domain with a non-zero function. There are three types of basis function: 1) local, 2) mid-range, and 3) global. For a local basis function, the non-zero part is a small portion of the design domain with a minimum overlap of functions. The downside of local basis function is the usage of several iterations to move boundaries significantly. This occurs when there is no smoothing regularization as changes in nodal values cannot displace material surfaces more than the size of a single element. Mid-range and global basis functions are similar to local basis function. However, mid-range function has a denser overlap and global basis function overlaps almost throughout the domain. Global basis function utilizes all design variables

in updating the surface of the material in the design domain. This leads to a faster rate of design change at the expense of higher computational cost. Despite its efficiency, finding an appropriate time step to prevent a larger change in the surface of the material is a challenge [77].

The optimization variable in LSF can also be defined in a scaling basis function or translating basis function. Scaling is widely used to parameterize LSF. It employs nodal values by applying a scale factor to the design variables. However, such interpolation scheme does not provide control over the LSF gradients when upper and lower bounds are not defined. Xing et al. proposed the translating basis function [85]. It provides basis function provides a fair control over the LSF gradient and length scale.

One-dimensional coordinate elements can be transformed using linear, quadric, and cubic basis function. For two-dimensional elements, the coordinates of the elements can be transformed using linear, and quadratic basis functions. The basis function can also consist of sub-functions such as piecewise and bilinear interpolation. Wang et al. developed radial basis functions (RBF) to produce smooth surface contours and continuous spatial gradient of LSF. Gomes et al. introduced the application of spectral parameterization in topology optimization using the Fourier series expansion [86]. Design variables of surface were replaced with coefficients of the Fourier series expansion. One advantage of this parameterization is the nucleation of new holes in surfaces. This prevents the occurrence of numerical instabilities such as the checkerboard. Spectral parameterization has been observed to be very efficient in optimizing periodic structures [77].

Figure 11 illustrates the various types of interpolation functions.

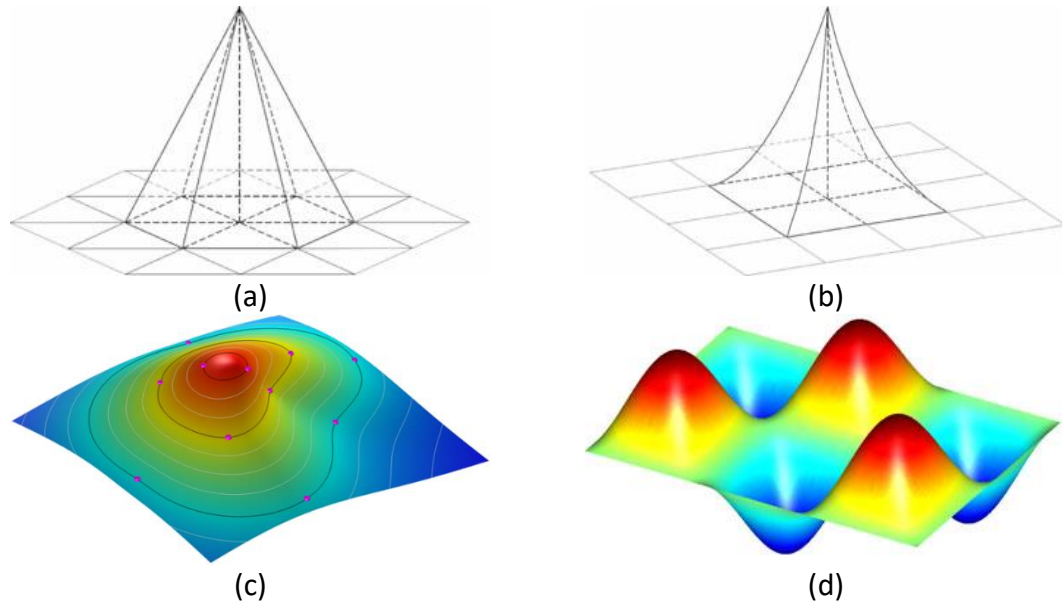


Figure 11. Various Types of Interpolation Functions: (a) Piecewise Linear Basis Function on 2D Domain Discretized by Triangles^[77], (b) Bi-Linear Basis Function on 2D Domain Discretized by Squares^[77], (c) Radial Basis Function Contour Plot^[87], and (d) Spectral Contour Plot^[88]

2.3.5.2 Updating the Level Set Function (LSF)

A general equation for motion of the LSF in three-spatial dimensions is defined by a mean curvature and represented in Equation 72:

$$\phi_t + H(\phi_x, \phi_y, \phi_z) \tag{72}$$

ϕ_t is an implicit LSF with respect to time, ϕ_x , ϕ_y , and ϕ_z represents LSF with respect to its x , y , and z coordinates. H can be a function of both space and time.

To describe the motion of a function, a normal velocity field is constructed. The velocity fields are developed to move optimization processes toward an optimum point in the design domain within the boundaries defined. This is to ensure the convergence for numerical model. Different velocity extensions have been proposed for different types of problems [77]. The extensions include: 1) normal, 2) natural, 3) Hilbertian, and 4) Helmholtz velocity

extensions. Normal velocity extension is a component of the velocity in a constant direction. Nucleation of new holes in the surface above the boundaries is not possible in sensitivity based LSF when the normal velocity is applied. Natural velocity extension does not need to solve additional partial differential equations (PDE) as they are constructed from shape gradients. However, natural velocity extension supports new nucleation of holes provided that the motion of the surface above the boundaries would no signed-distance re-initialized [77, 89]. In 2006, De Gournay proposed the Hilbertian velocity extension [90]. This method introduced a scalar product to calculate the descent direction to regularize the velocity of the LSF. Yamasaki et al. used Helmholtz-type PDE to smoothen sensitivities in the computation of normal velocities in the LSF [91]. Although the velocity extension associates velocity to the shape sensitivity, it does not support the nucleation of new holes.

Hamilton-Jacobi equation is a common approach that is used to update LSF as it represents a general equation for motion by mean curvature defined in three-spatial dimensions. The first order differential of the Hamilton-Jacobi equation can be evaluated by Equation 73:

$$\frac{\partial \phi}{\partial t} + V \|\nabla \phi\| \tag{73}$$

$\partial \phi$ represents the change in LSF over a period of time (∂t), V is a velocity field, and $\|\nabla \phi\|$ is the modulus of gradient. The gradient of the implicit LSF is defined as Equation 74:

$$\nabla \phi = \left(\frac{\partial \phi}{\partial x} \quad \frac{\partial \phi}{\partial y} \quad \frac{\partial \phi}{\partial z} \right) \tag{74}$$

2.3.6 Numerical Instabilities

In topology optimization problems several numerical instabilities may occur due to the complexity of the problems under consideration. The common numerical instabilities encountered could be classified into three categories: 1) checkerboard, 2) mesh dependency, and 3) local minima [92].

2.3.6.1 Checkerboard

Figure 12 illustrates the formation of elements in a checkerboard pattern (i.e., an alternating solid and void pattern). Optimized structures with checkerboard patterns lack connectivity and cannot be manufactured. To solve the checkerboard instability several heuristic methods can be implemented such as: density filters [63], sensitivity filters [92], and perimeter control [93]. Huang et al. illustrated that choosing an appropriate perimeter control method is difficult [45]. Therefore, the sensitivity filter scheme represents the most preferable methodology due to its ease of implementation.



Figure 12 Optimized beam with checkerboards

The sensitivity filter on an element level is defined by Equation 75:

$$\frac{\widehat{\partial f}}{\partial \rho_k} = (\rho_k)^{-1} \frac{1}{\sum_{i=1}^N \widehat{H}_i} \sum_{i=1}^N \widehat{H}_i \rho_i \frac{\partial f}{\partial \rho_i} \quad 75$$

where \widehat{H}_i is a convolution operator (weight factor) and is defined by Equation 76:

$$\widehat{H}_i = r_{min} - \text{disk}(k, i), \{ \in N \mid \text{dist}(k, i) \leq r_{min} \} \quad 76$$

where $k = 1, \dots, N$, $\text{dist}(k, i)$ is the center-to-center distance between the k^{th} and i^{th} element.

While r_{min} is filter scheme to account for neighboring elements affecting the sensitivity of an element.

For ETO methodologies, the filtering scheme is applied on the nodal level. Therefore, the nodal sensitivity can be computed as the weighted average of the neighboring element's sensitivity values as illustrated as given in Equation 77:

$$\alpha_j^n = \sum_{i=1}^M w_i \alpha_i^e \quad 77$$

where M is the number of elements surrounding the j th node, w_i is the weight factor of the i th element (1 or 0.001). w_i can be defined by Equation 78:

$$w_i = \frac{1}{M-1} \left(1 - \frac{r_{ij}}{\sum_{i=1}^M r_{ij}} \right) \quad 78$$

where r_{ij} is the center-to-center distance between the i th element and the j th node.

Equation 78 has a greater influence of the sensitivity number of elements with a small center-to-center distance. The filtering scheme is applied on the elements sensitivity by utilizing a length scale radius r_{min} . r_{min} is a constant value that is used to scan and identify neighboring nodes that affects the sensitivity of the i th element. A value of r_{min} greater than the mesh sizes is recommended to ensure more than one element is considered during smoothing. This is to consider the densities and sensitivities of the surrounding elements and eliminate any local extremes. The average sensitivity number of an element within the radius (r_{min}) is calculated by Equation 79:

$$\alpha_i = \frac{\sum_{j=1}^k w(r_{ij}) \alpha_j^n}{\sum_{j=1}^k w(r_{ij})} \quad 79$$

where k is the total number of nodes with the region of the radius and $w(r_{ij})$ is the linear weight factor. The linear weight factor $w(r_{ij})$ can be computed by Equation 80:

$$w(r_{ij}) = r_{min} - r_{ij} \quad 80$$

2.3.6.2 Mesh Dependency

In FEA, it is assumed that an increase in the mesh density of a numerical problem would lead to more accurate results. However, that is not the case in mesh dependency problems. Mesh dependency problem is the differences in layout of optimized domain (material distribution) due to differences in mesh densities for the same numerical problem. This leads to inaccurate results as the densities and structural stiffness is dependent on the number of elements used.

Sensitivity filters and relaxation can be implemented to assist in eliminating the effect of the mesh density [10, 92, 94]. But these methodologies do not solve non-convergence issues. A numerical solution might not converge due to the oscillations that may occur in the calculations of the objective function. Huang et al. proposed averaging the element's sensitivity number of current and previous iterations to attain stability in the optimization process. The averaging scheme is computed by Equation 81:

$$\alpha_i = \frac{\alpha_i^k + \alpha_i^{k-i}}{2} \quad 81$$

where k represents the current iteration.

2.36.3 Local Minima

The local minima instability is similar to the mesh dependency instability; however, the inaccurate results would depend on the optimization parameters (such as: filter radius and moving limits in sensitivity). To ensure convergence of a gradient based optimization problem, the continuation method (i.e., varying density from 0 to 1) and a non-linear material interpolation scheme (with a penalization factor greater than 1, preferably 3) can be implemented [92]

CHAPTER 3

PROBLEM FORMULATION

To compare the performance of the three most known compliance-based topology optimization algorithms (i.e., SIMP, BESO, and LSM), the Messerschmidt-Bölkow-Blohm (MBB) model was used. The MBB model is a well-known simply supported beam with a three-point loading configuration that is often used to benchmark topology optimization problems.

Figure 13 illustrates a schematic drawing of the MBB beam. In all simulations, A992 steel material properties were assigned, with an elastic modulus of 200GPa (29,000ksi), and a Poisson's ratio (ν) of 0.3. The simulated beams had a length of 1000mm, and a height of 250mm. The impact of the thickness on the algorithm was also investigated by considering 20mm, 40mm and 60mm thick beams. A maximum load of 861.8kN was applied, representing a maximum displacement of 1.149mm, for the beam with a 60mm thickness.

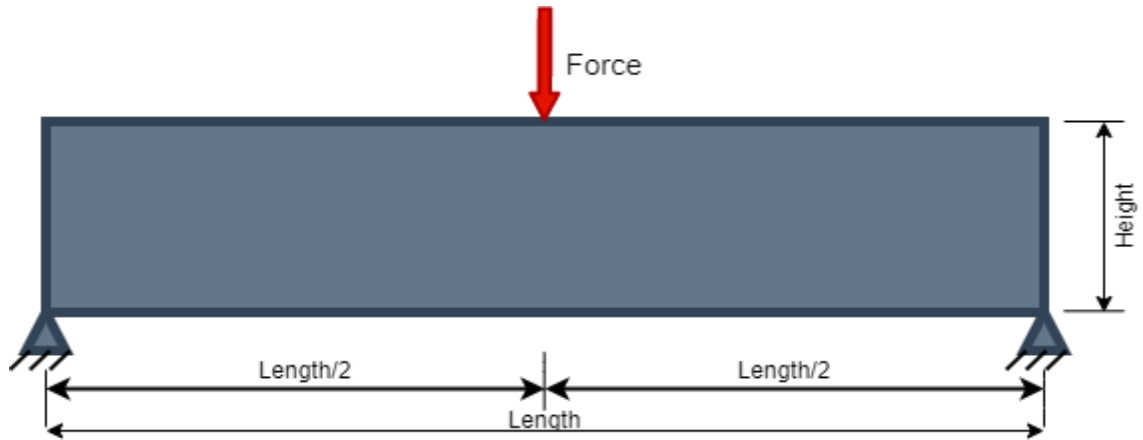


Figure 13. Illustration of the Messerschmidt-Bölkow-Blohm (MBB) model

A total of 61 simulations were performed with 16 simulations for each optimization technique of SIMP and LSM. While 26 simulations were performed for beams optimized using the BESO. Group 1 which consisted of simulations 1 to 5, was considered to investigate the effect of mesh density with respect to the algorithms on the optimized structure. Group 2 that consisted of simulations 4, 6 and 7, was conducted to study the effect of the beam thickness on the optimized structure. Group 3, consisted of simulations 4, 8 and 9, was used to investigate the effect of the filter radius on the optimized structure solved by SIMP and BESO. For the structures optimized using LSM, the effect of the size of holes that are nucleated was investigated. Group 4, that consisted of simulations 4, 10, and 11, was deployed to study the effect of the penalization factor on the performance of the optimization algorithms. Group 5, consisted of simulations 4, and 12 to 16, was used to study the effect of the desired volume fraction on the performance of the optimized structure. Group 6 that consisted of simulations 4, and 17 to 23 was implemented to investigate the effect of the removal and addition ratios for structures optimized by the BESO. Finally, Group 7 that consisted of simulation 4 and simulations 24 to 26 was

considered study the effect of the convergence criteria for structures optimized by BESO. For structures optimized with LSM, a time-step of 0.5, a delta (Δ) of 10 iterations were used to update the velocities. A moving constant (μ) of 20 for reducing the volume was chosen for optimizing the structure using LSM. Finally, Table 1 provides the parameters used in each simulation

Table 1. Simulation Parameters for MBB Optimized using SIMP, BESO and LSM

Common Parameters						SIMP and BESO only	BESO only			LSM only
Simulation	Elements in X	Elements in Y	Thickness (mm)	Penal	Volume Fraction	Rmin	ERR	Armax	Tau	R_holes
1	200	100	20	2	0.5	1	0.04	0.02	0.001	0.1
2	200	75	20	2	0.5	1	0.04	0.02	0.001	0.1
3	200	50	20	2	0.5	1	0.04	0.02	0.001	0.1
4	150	50	20	2	0.5	1	0.04	0.02	0.001	0.1
5	100	50	20	2	0.5	1	0.04	0.02	0.001	0.1
6	150	50	40	2	0.5	1	0.04	0.02	0.001	0.1
7	150	50	60	2	0.5	1	0.04	0.02	0.001	0.1
8	150	50	20	2	0.5	1.5	0.04	0.02	0.001	0.2
9	150	50	20	2	0.5	2	0.04	0.02	0.001	0.5
10	150	50	20	4	0.5	1	0.04	0.02	0.001	0.1
11	150	50	20	6	0.5	1	0.04	0.02	0.001	0.1
12	150	50	20	2	0.6	1	0.04	0.02	0.001	0.1
13	150	50	20	2	0.7	1	0.04	0.02	0.001	0.1
14	150	50	20	2	0.75	1	0.04	0.02	0.001	0.1
15	150	50	20	2	0.8	1	0.04	0.02	0.001	0.1
16	150	50	20	2	0.9	1	0.04	0.02	0.001	0.1
17	150	50	20	2	0.5	1	0.01	0.01	0.001	
18	150	50	20	2	0.5	1	0.05	0.05	0.001	
19	150	50	20	2	0.5	1	0.1	0.1	0.001	
20	150	50	20	2	0.5	1	0.05	0.02	0.001	
21	150	50	20	2	0.5	1	0.1	0.02	0.001	
22	150	50	20	2	0.5	1	0.02	0.05	0.001	
23	150	50	20	2	0.5	1	0.02	0.1	0.001	

24	150	50	20	2	0.5	1	0.04	0.02	0.0001	
25	150	50	20	2	0.5	1	0.04	0.02	0.00001	
26	150	50	20	2	0.5	1	0.04	0.02	0.00001	

CHAPTER 4

NUMERICAL APPROACH

4.1 *Solid Isotropic Material/Microstructure with Penalization (SIMP)*

A MATLAB code developed by Sigmund et al. constituted the basis for the structures optimized using SIMP [67]. The MATLAB script utilizes optimal criteria (OC) sensitivity method together with a mesh-dependency filter. The script is initiated by assigning the design variables with a prescribed volume fraction. The FEA is then initiated to solve for displacements (U) and stiffnesses (K). After the computation of elements' stiffnesses in Equation 8, the assembly equation used in Equation 15 is penalized to implement the penalization factor. Hence, the design variable (ρ_e) becomes a factor of the stiffness as defined in Equation 82:

$$K_e(\rho_e) = x^P [KE] \quad 82$$

K_e represents the element's effective stiffness, ρ_e is a design variable, x is the element's density, and KE is the global stiffness of the structure. As a result, the displacement $\{U\}$ can be computed as given in Equation 83.

$$\{U\} = \frac{K_e(\rho_e)}{\{F\}} \quad 83$$

Subsequently, the element's compliance (objective function) can be then calculated by Equation 84

$$C_e = x^P U_e^T K E U_e \quad 84$$

C_e is the element's compliance, x is the element's density, P is the penalization factor, U_e^T is the transpose of the element's displacement. The sensitivity of the objective function can be calculated by Equation 84:

$$\partial C = -P x^{(P-1)} U_e^T K E U_e \quad 85$$

The mesh-dependency filter was then applied to the sensitivity function using Equation 86:

$$\frac{\partial \widehat{c}}{\partial \rho_e} = (\rho_e)^{-1} \frac{1}{\sum_{i=1}^N \widehat{H}_i} \sum_{i=1}^N \widehat{H}_i \rho_e \frac{\partial c}{\partial \rho_e} \quad 86$$

Finally, the design variables (i.e., densities) are updated using the optimal criteria scheme represented in Equation 31. This iterative process continues until the convergence criterion is satisfied. A flowchart of the procedure implemented in the algorithms is presented in Figure 14

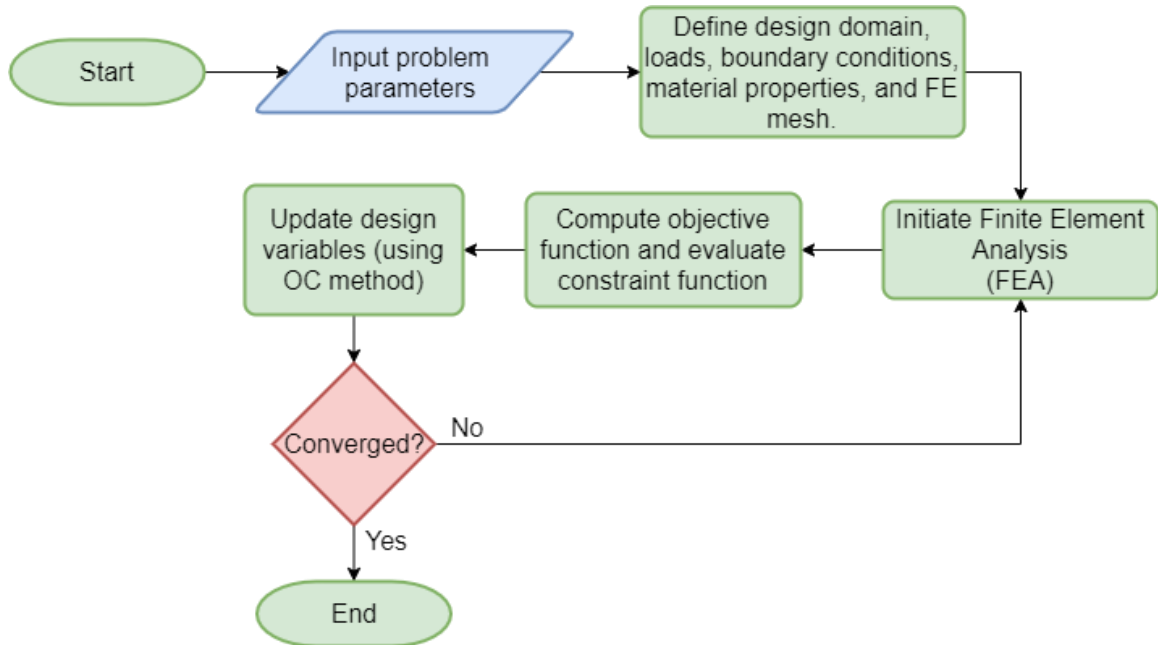


Figure 14. Flowchart Representing the Procedure for SIMP

4.2 Evolutionary Topology Optimization (ETO)

4.2.1 Evolutionary Structural Optimization (ESO)

The ESO optimization scheme is an application approach to achieve an optimized structure with a predefined compliance or a displacement limit. The iteration terminates upon reaching the predefined limit irrespective of the other factors. Evolutionary rejection ratio (ERR) is introduced prior to the initiation of the MATLAB script to implement the removal of elements. Likewise, the prescribed limit for either compliance or displacement is defined (i.e., a convergence limit). The design domain is assigned a volume of 1 (as elements will be gradually removed during each iteration). The assigned volume can be defined by Equation 87:

$$x(1:nely, 1:nelx) = 1 \quad 87$$

The mean compliance of each element is computed by Equation 88 after the calculation of the element's stiffness and nodal displacements. Unlike SIMP, ETO is a discrete method (no intermediate densities). The sensitivity function of the objective function is calculated by Equation 89:

$$C = \frac{1}{2} x^P U_e^T K E U_e \quad 88$$

$$\alpha_e = -\frac{1}{P} \frac{\partial C}{\partial x_e} = \begin{cases} \frac{1}{2} \times x^P \times U_e^T \times K E \times U_e, \text{ when } x = 1 \\ \frac{\rho_{min}^{P-1}}{2} U_e^T \times K E \times U_e, \text{ when } x = 0 \end{cases} \quad 89$$

The mesh dependency filter defined in Equation 86 is implemented. Then the elements' sensitivities are sorted in a descending order to eliminate elements with the

lowest sensitivities. The number of elements to be removed is determined by the pre-defined ERR and can be calculated from Equation 90:

$$ERR = \frac{\text{number of elements removed}}{\text{Total number of elements in initial model}} \quad 90$$

$$\text{elements removed} = ERR \times \text{Total elements in initial model} \quad 91$$

Since ETO is a discrete method, a bilinear surface smoothing scheme based on nodal density and sub-element interpolation is applied to achieve a uniform density from elements to nodes.

4.2.2 Bi-Evolutionary Structural Optimization (BESO)

Unlike ESO, BESO simultaneously removes and adds elements. Solid elements with low sensitivity number are removed while void elements with high sensitivity numbers are added. Prior to the initiation of the MATLAB script, both ERR and AR_{\max} are defined. For elements to be added, AR_{\max} is assigned a value greater than 1%. The MATLAB script is initiated by defining design variables and structural volume as in Equations 92 and 93:

$$x(1:nely, 1:nelx) = 1 \quad 92$$

$$vol = 1 \quad 93$$

The volume fraction of the structure can be determined by Equation 94 at the end of each iteration.

$$vol^k = \begin{cases} \max(Vol(1 - ER), V_o) \\ \min(Vol(1 - ER), V_o) \end{cases} \quad 94$$

vol^k is the structural volume of the k^{th} iteration, ER is the evolutionary ratio, and V_o is the volume fraction. The FEA is then initiated to determine both elements stiffness and nodal displacements. The mean compliance can be then calculated using Equation 95:

$$C = \frac{1}{2} x^P U_e^T K E U_e \quad 95$$

The sensitivity function is then computed through Equation 96:

$$\alpha_e = -\frac{1}{P} \frac{\partial C}{\partial x_e} = \begin{cases} \frac{1}{2} x^P U_e^T K E U_e, \text{ when } x = 1 \\ \frac{\rho_{min}^{P-1}}{2} U_e^T K E U_e, \text{ when } x = 0.001 \end{cases} \quad 96$$

α_e is the sensitivity number, P is the penalization factor, and x represents the design variable. The defined mesh dependency filter is applied followed by an averaging scheme as given in Equation 97:

$$dc_k = \frac{dc^{k-1} + dc^k}{2} \quad 97$$

To remove and add elements, a sensitivity threshold is defined by Equation 98:

$$dC_{solids} = vol^k \times dC_{all} \quad 98$$

dC_{solids} is the number of elements with significant sensitivities greater than the threshold and dC_{all} represents the sensitivity of all elements. The volume density of the element is then defined by Equation 100:

$$\text{if } dC_i > dC_{threshold}, x_i = 1 \quad 99$$

$$\text{else, } x_i = x_{min} \quad 100$$

where dC_i and x_i are the sensitivity and density of an element, respectively. x_{min} is the minimum density, usually taken as 0.001 to represent a soft density for voids. At this point, there is a need to check if additional elements are required in the design domain in relation to a prescribed maximum addition ratio (AR_{max}). The number of elements to be added is equal to the difference between the current and previous number of solid elements in the

design domain. The process given in Equations 69 for checking the additional element added is repeated iteratively until convergence criterion is satisfied as defined in Equation 70. A flowchart representing the iterative process of the BESO is presented in Figure 15.

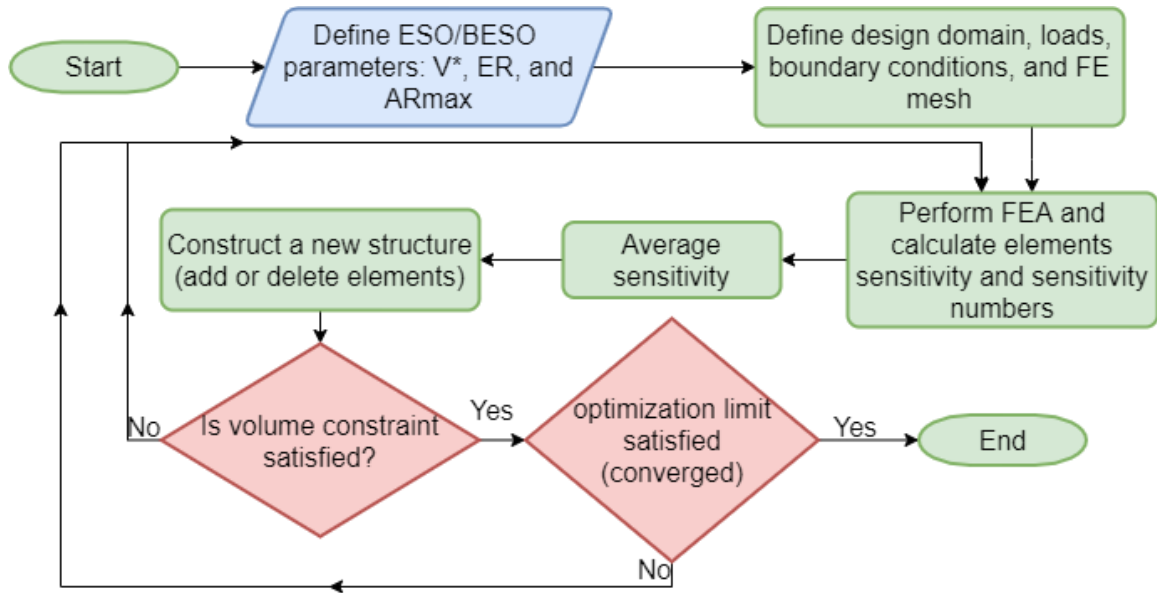


Figure 15. Flowchart Representing the BESO Algorithm Implemented

4.2.3 Bilinear Interpolation

In this scheme, the element densities are replaced with nodal densities using a bilinear interpolation scheme. Element nodes were group into three categories based on the location of the nodes as illustrated in

Figure 16. The three categories are: 1) corner nodes such as N1, 2) edge nodes such as N2, and 3) center nodes such as N3.

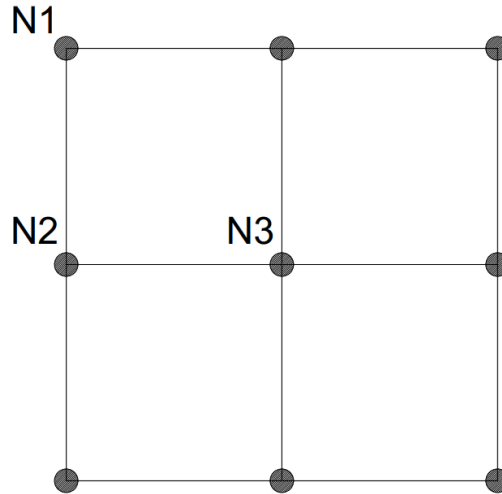


Figure 16. Nodal Classification Based on Its Location in a Structure

The nodal densities can be calculated by Equation 101:

$$\rho_n = \frac{\sum_1^n \rho_e v_e}{\sum_1^n v_e}, (n = 1,2,3,4) \quad 101$$

ρ_n is the nodal density, ρ_e is the design variable (densities), n is the number of adjacent elements to the node, and v_e is the element's volume. Therefore, each nodal density could be computed based on its location by Equations 102 to 104:

Corner Node:

$$\rho_n = \rho_{1e} \quad 102$$

Edge Node:

$$\rho_n = \frac{1}{2}(\rho_{1e} + \rho_{2e}) \quad 103$$

Center Node:

$$\rho_n = \frac{1}{4}(\rho_{1e} + \rho_{2e} + \rho_{3e} + \rho_{4e}) \quad 104$$

For a structure that is subdivided into a 20-by-20 nodes, with 4-nodal elements would have the densities of the interior points calculated by Equations 105 and 106 using the bilinear interpolation.

$$\rho_c(\xi, \eta) = \sum_{n=1}^4 N_i(\xi, \eta) \rho_{n_i}(x) \quad 105$$

$$\rho_c(\xi, \eta) = N_1(\xi, \eta) \rho_{n1}(x) + N_2(\xi, \eta) \rho_{n2}(x) + N_3(\xi, \eta) \rho_{n3}(x) + N_4(\xi, \eta) \rho_{n4}(x) \quad 106$$

where ρ_c is the density at a point, $N_i(\xi, \eta)$ is the bilinear function for shape function, and ρ_{n_i} is the nodal density. Song et al. investigated the effect of interpolation scheme on the results of topology optimization [95]. The results illustrated that extreme interpolation may remove essential elements, while soft interpolation may result into a highly dense structure with singularities.

Figure 17 illustrates the effect of smoothing the surface using iso-line values ranging from 0.1 to 0.9 [95].



Figure 17. Effect of surface smoothing with an iso-line value of: (a) 0.1, (b) 0.5, (c) 0.7 and (d) 0.9^[95]

4.3 Level Set Method (LSM)

The MATLAB script used in this section was based on the work of Wei et al. [96]. The adopted script uses the extended level set method proposed by Wang et al. [97]. The LSM scheme employs the radial basis function (RBF) to define the smoothness of the surfaces. The script was modified to consider the penalization factor. Since LSF utilizes nodes and not quad-linear elements, a “node-to-element” script has been written to map the nodal densities into elements densities for further analysis. The RBF can be expressed by Equation 107:

$$\varphi_i(x) = \varphi(\|x - x_i\|), x_i \in D \quad 107$$

where x is the position of the nodes. The implemented RBF uses the multiquadric interpolation scheme due to its excellent performance and can be expressed by Equation 108:

$$\varphi_i(x) = \sqrt{(x - x_i)^2 + C_i^2} \quad 108$$

where C is a constant shape parameter, normally assigned a smaller value to ensure stability of algorithm. The multiquadric spline is to interpolate the LSF ($\phi(x)$) which can be expressed by Equation 109:

$$\phi(x) = \sum_{i=1}^N \alpha_i \varphi_i(x) + p(x) \quad 109$$

where α_i is the expansion coefficient of RBF and $p(x)$ is the 1st degree polynomial that is introduced to account for the linear and constant portions of $\phi(x)$. Also, it ensures the positive definiteness of the solution [98]. The $p(x)$ of the model is expressed by Equation 110:

$$p(x) = p_0 + p_1x + p_2y + p_3z \quad 110$$

where p_0 , p_1 , and p_2 are the coefficients of the polynomial. Therefore, Equation 109 can be re-written as given in Equation 111:

$$H\alpha = f \quad 111$$

where α and f are expressed by Equations 112 and 113:

$$\alpha = [\alpha_1 \cdots \alpha_N \ p_0 \ p_1 \ p_2 \ p_3]^T \in \mathbb{R}^{N+4} \quad 112$$

$$f = [f_1 \cdots f_N \ 0 \ 0 \ 0 \ 0]^T \in \mathbb{R}^{N+4} \quad 113$$

The generalized expansion coefficients can then be expressed by Equations 114 and 115:

$$\alpha = H^{-1}f \quad 114$$

$$H = \begin{bmatrix} A & P \\ P^T & 0 \end{bmatrix} \in \mathbb{R}^{(N+4) \times (N+4)} \quad 115$$

where A and P are computed by Equations 116 and 117:

$$A = \begin{bmatrix} \varphi_1(x_1) & \cdots & \varphi_N(x_1) \\ \vdots & \ddots & \vdots \\ \varphi_1(x_N) & \cdots & \varphi_N(x_N) \end{bmatrix} \in \mathbb{R}^{N \times N} \quad 116$$

$$P = \begin{bmatrix} 1 & x_1 & y_1 & z_1 \\ \vdots & \vdots & \vdots & \vdots \\ 1 & x_N & y_N & z_N \end{bmatrix} \in \mathbb{R}^{N \times 4} \quad 117$$

Equation 109 can then be re-written to be expressed as given in Equation 118 based on the expansion coefficients.

$$\phi(x) = \Phi^T(x) \alpha \quad 118$$

Expanding Equation 118 will result into Equation 119:

$$\phi(x) = [\varphi_1(x) \cdots \varphi_N(x) \ 1 \ x \ y \ z]^T \in \mathbb{R}^{(N+4) \times 1} \quad 119$$

The objective function (i.e., minimization of the compliance) can be then defined by Equation 120:

$$J(u, \phi) = \int_D (\varepsilon(u)) : C : \varepsilon(u) H(\phi) d\Omega \quad 120$$

The objective function is subjected to some constraints as defined by Equations 121 to 124:

$$a(u, v, \phi) = l(v, \phi) \forall (v, \phi) \quad 121$$

$$G(\phi) = \int_D H(\phi) d\Omega - V_{max} \leq 0 \quad 122$$

$$u = u_0 \quad 123$$

$$C : \varepsilon(u) \cdot n = \tau \quad 124$$

where $a(u, v, \phi)$ and $l(v, \phi)$ represent the virtual work of the internal forces and the external surfaces, respectively. $G(\phi)$ is a shape gradient constraint to limit the material usage. H is the Heaviside function to define solids and voids. u represents nodal displacements, C is the Hook elasticity tensor, ε is the strain tensor, and τ is the surface traction.

Since the LSM is an implicit boundary method, it involves the motion of evolving surfaces with respect to time. The Hamilton-Jacobi PDE using a capturing Eulerian approach for conventional LSF can be defined by Equation 125:

$$\frac{\partial \phi}{\partial t} + v_n \cdot |\nabla \phi| = 0 \quad 125$$

where the normal velocity (v_n) is defined by Equation 126:

$$v_n = v \cdot \frac{\nabla \phi}{|\nabla \phi|} \quad 126$$

The RBF Equation 118 can be re-written in a time dependent format as expressed by Equation 127:

$$\boldsymbol{\phi} = \boldsymbol{\phi}(x, t) = \boldsymbol{\phi}^T(x)\boldsymbol{\alpha}(t) \quad 127$$

Substituting Equation 127 into the Hamilton-Jacobi PDE. Equation 128 to 135 can be deduced:

$$\boldsymbol{\phi}^T \frac{d\boldsymbol{\alpha}}{dt} + v_n |(\nabla\boldsymbol{\phi})^T \boldsymbol{\alpha}| = \mathbf{0} \quad 128$$

$$|(\nabla\boldsymbol{\phi})^T \boldsymbol{\alpha}| = \left[\left(\frac{\partial\boldsymbol{\phi}^T}{\partial x} \boldsymbol{\alpha} \right)^2 \quad \left(\frac{\partial\boldsymbol{\phi}^T}{\partial y} \boldsymbol{\alpha} \right)^2 \quad \left(\frac{\partial\boldsymbol{\phi}^T}{\partial z} \boldsymbol{\alpha} \right)^2 \right]^{1/2} \quad 129$$

$$\frac{\partial\boldsymbol{\phi}}{\partial x} = \left[\frac{\partial\varphi_1}{\partial x} \quad \dots \quad \frac{\partial\varphi_N}{\partial x} \quad \mathbf{0} \quad \mathbf{1} \quad \mathbf{0} \quad \mathbf{0} \right]^T \in \mathbb{R}^{(N+4) \times 1} \quad 130$$

$$\frac{\partial\boldsymbol{\phi}}{\partial y} = \left[\frac{\partial\varphi_1}{\partial y} \quad \dots \quad \frac{\partial\varphi_N}{\partial y} \quad \mathbf{0} \quad \mathbf{1} \quad \mathbf{0} \quad \mathbf{0} \right]^T \in \mathbb{R}^{(N+4) \times 1} \quad 131$$

$$\frac{\partial\boldsymbol{\phi}}{\partial z} = \left[\frac{\partial\varphi_1}{\partial z} \quad \dots \quad \frac{\partial\varphi_N}{\partial z} \quad \mathbf{0} \quad \mathbf{1} \quad \mathbf{0} \quad \mathbf{0} \right]^T \in \mathbb{R}^{(N+4) \times 1} \quad 132$$

$$\frac{\partial\varphi_1}{\partial x} = \frac{x - x_i}{\sqrt{(x - x_i)^2 + (y - y_i)^2 + (z - z_i)^2 + c_i^2}}, \quad i = 1, \dots, N \quad 133$$

$$\frac{\partial\varphi_1}{\partial y} = \frac{y - y_i}{\sqrt{(x - x_i)^2 + (y - y_i)^2 + (z - z_i)^2 + c_i^2}}, \quad i = 1, \dots, N \quad 134$$

$$\frac{\partial\varphi_1}{\partial z} = \frac{z - z_i}{\sqrt{(x - x_i)^2 + (y - y_i)^2 + (z - z_i)^2 + c_i^2}}, \quad i = 1, \dots, N \quad 135$$

The side constraints are then introduced to assure that the generalized coefficients $\boldsymbol{\alpha}$ is solvable. The constraints are represented by Equation 136 taking into consideration time-dependent interpolation.

$$\sum_{i=1}^N \dot{\alpha}(t) = 0, \sum_{i=1}^N \dot{\alpha}(t)x_i = 0, \sum_{i=1}^N \dot{\alpha}(t)y_i = 0, \sum_{i=1}^N \dot{\alpha}(t)z_i = 0 \quad 136$$

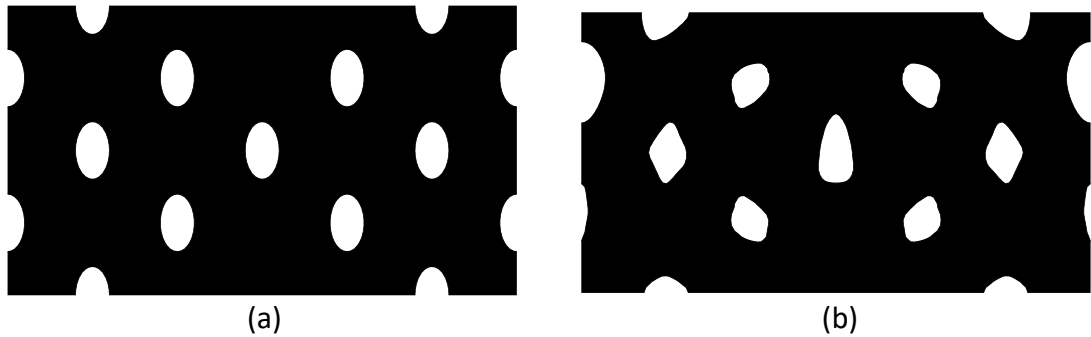
Introducing the side constraints into Equation 111, the ordinary differential equation can be expressed as given in Equation 137:

$$\frac{d\alpha}{dt} + \mathbf{B}(\alpha) = \mathbf{0} \quad 137$$

where $B(\alpha)$ represents the updated velocity at a time step of the surface leading to the movement of surfaces in the LSM and can be computed by Equation 138:

$$\mathbf{B}(\alpha) = \begin{bmatrix} v_n^e(x_1)|(\nabla\phi^T(x_1))\alpha| \\ \vdots \\ v_n^e(x_N)|(\nabla\phi^T(x_N))\alpha| \\ \mathbf{0} \\ \mathbf{0} \\ \mathbf{0} \\ \mathbf{0} \end{bmatrix} \in \mathbb{R}^{(N+4) \times 1} \quad 138$$

Figure 18 illustrates the “metamorphosis” of the LSM in solving a simple beam problem. In the scheme adopted, holes are nucleated at the initial stage of the iteration (iteration 1). The generative layout of the topology optimized beam is developed via the velocity of LSF and the movement of surfaces.



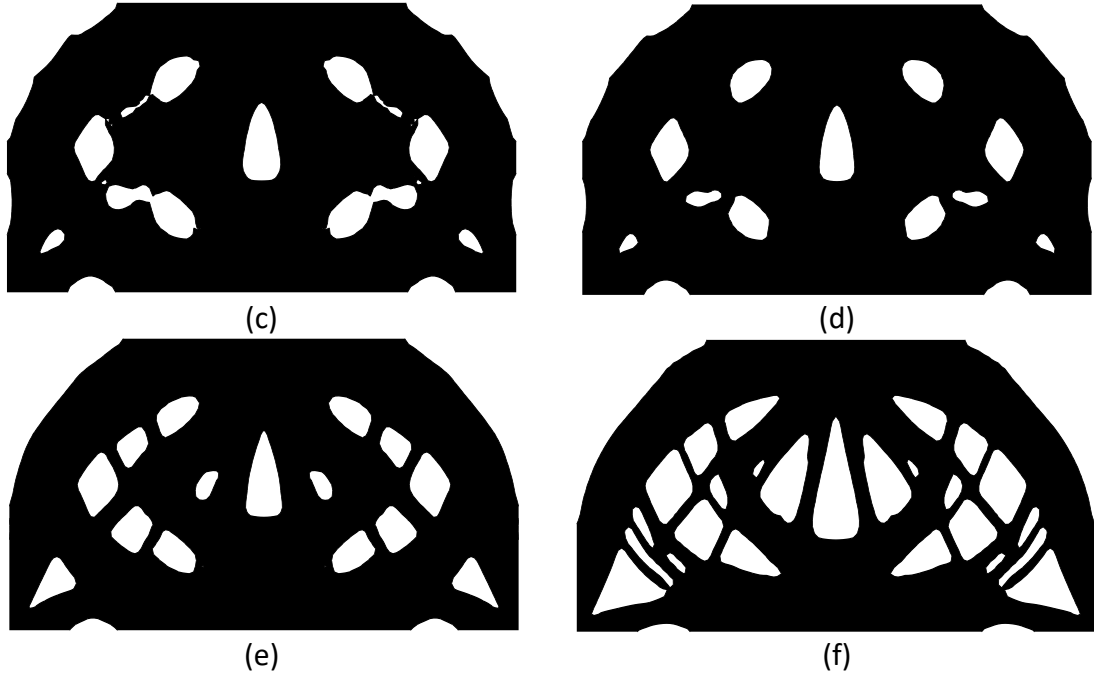


Figure 18. Illustration of the LSM procedure for solving a simple beam problem

CHAPTER 5

RESULTS AND DISCUSSION

5.1 Mesh Density Effect

Figure 20 illustrates the density plots of beams with different mesh densities. Structures optimized using SIMP revealed checkerboard numerical instabilities irrespective of the mesh density. Nonetheless, the design domain with a fine mesh provided the most accurate results (i.e., densities, compliance, and displacement). This reinforces the necessity of a well-dense domain discretization in order to reach an accurate and a representative solution. However, a dense mesh increases the computational cost (RAM usage) and does not always translate into computational time. Despite this, the mesh density exhibited an insignificant effect on the material distribution for structures optimized by the SIMP models as seen in Figure 19.

It is worth noting that the smallest compliance was achieved for structures optimized using LSM. This can be attributed to the Hook elasticity tensor factor in the formulation of the compliance. The ratio of the compliance of the structures with the coarse mesh to structures with a dense mesh was 2.55%, 8.99% and 3.73%, for optimization using SIMP, BESO, and LSM, respectively. The results suggest that a coarse mesh can be used for acquiring good results with a small computational cost. It should be noted that models with 999 iterations were terminated due to the oscillation of the numerical solution

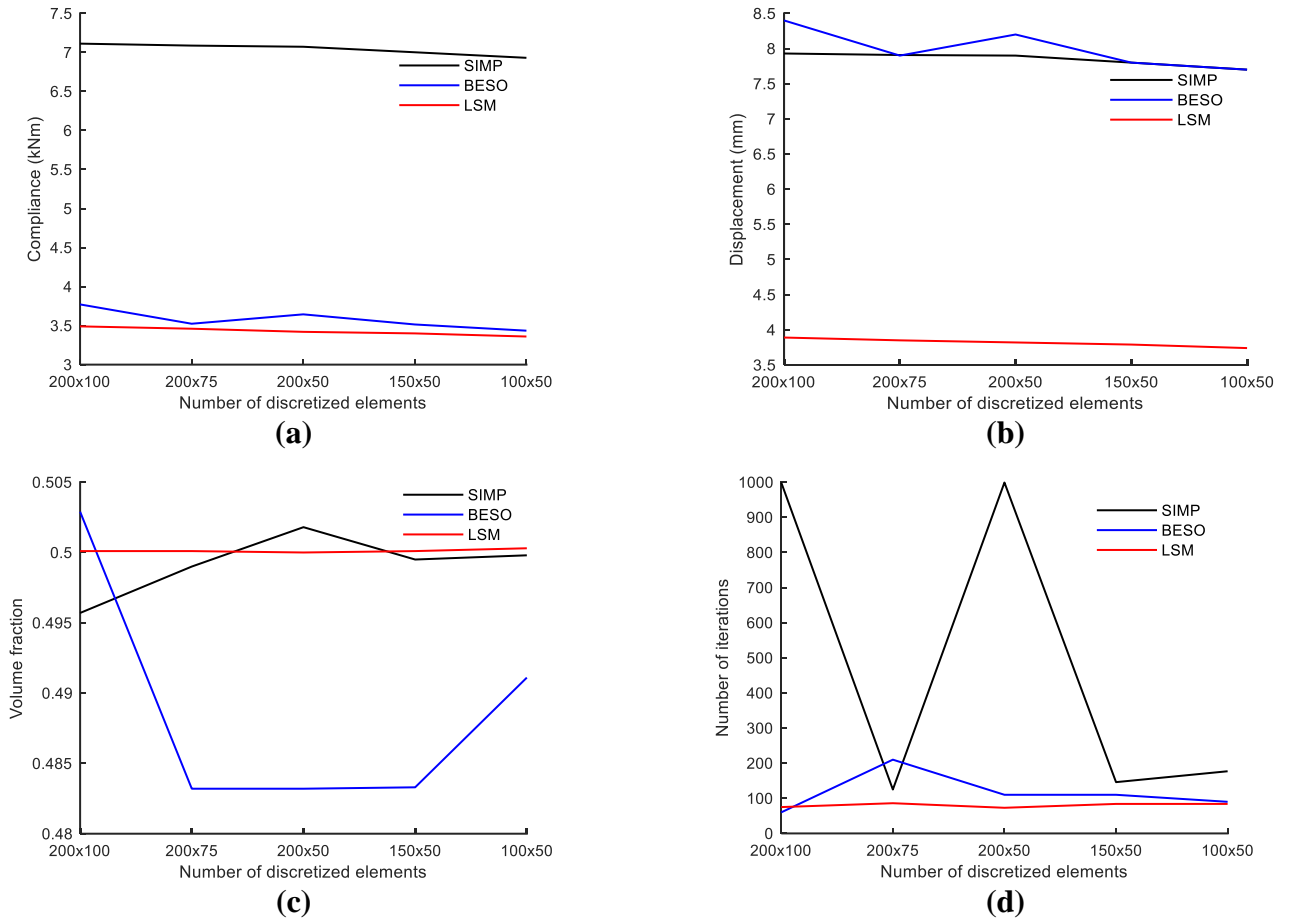


Figure 19 Results plot for different number of discretized elements: (a) compliance (kNm), (b) displacement (mm), (c) volume fraction, (d) number of iterations of SIMP, BESO and LSM models

SIMP



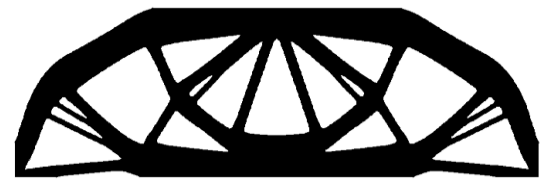
(a)

BESO

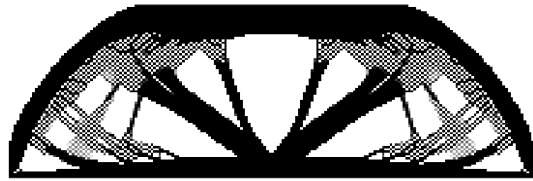


(b)

LSM



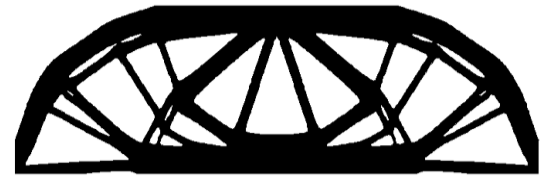
(c)



(d)



(e)



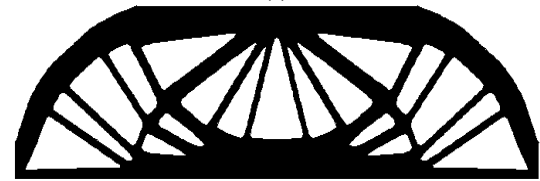
(f)



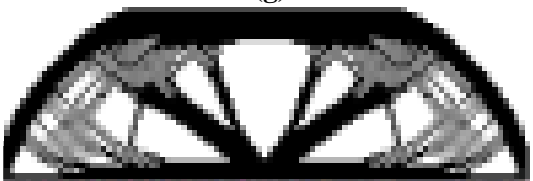
(g)



(h)



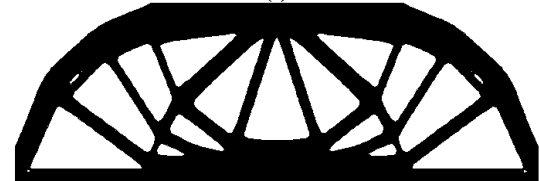
(i)



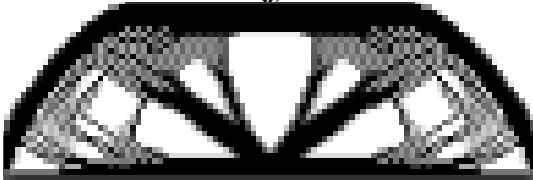
(j)



(k)



(l)



(m)



(n)

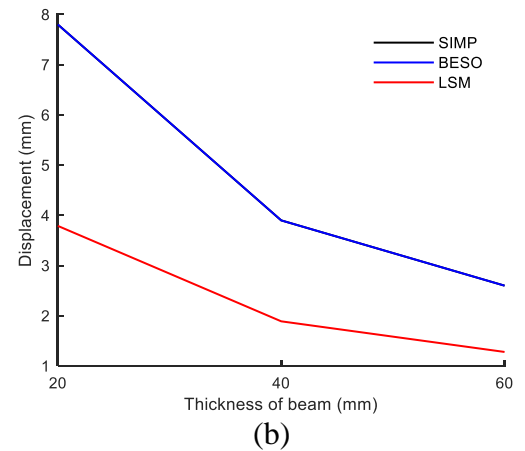
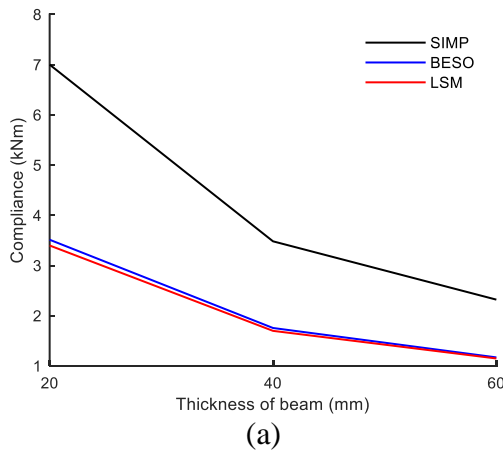


(o)

Figure 20 Plots of different mesh densities: (a), (b), and (c) represents 200×100 mesh densities of SIMP, BESO, and LSM, respectively. (d), (e), and (f) represents 200×75 mesh densities of SIMP, BESO, and LSM, respectively. (g), (h), and (i) represents 200×50 mesh densities of SIMP, BESO, and LSM, respectively. (j), (k), and (l) represents 150×50 mesh densities of SIMP, BESO, and LSM, respectively. (m), (n), and (o) represents 100×50 mesh densities of SIMP, BESO, and LSM, respectively.

5.2 Effect of Section Thickness

Figure 22 demonstrate that the change in thickness does not affect distribution of material for a structure optimized using SIMP and BESO. However, the thickness of the structure has an impact on the optimal solution reached by LSM. This can be contributed to the fact the LSM considers the boundaries and surfaces in a design domain. It was observed that the structure with a thickness of 60 mm had an excellent distribution of material for the load applied. Additionally, the performance (i.e., displacement and compliance) of all the optimized beams improved with increasing the thickness. The compliance values were the same for structures optimized using BESO and LSM. Also, structures optimized using SIMP and BESO recorded the same displacement values.



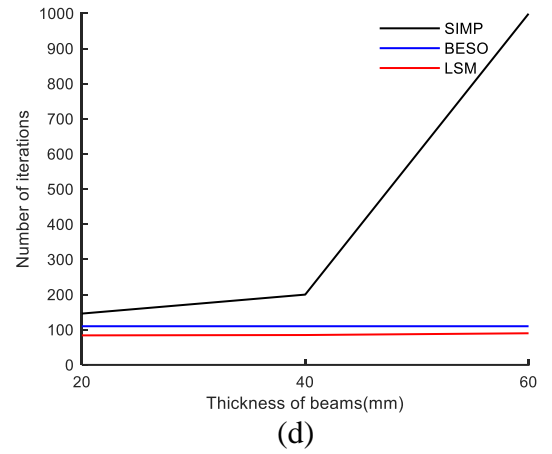
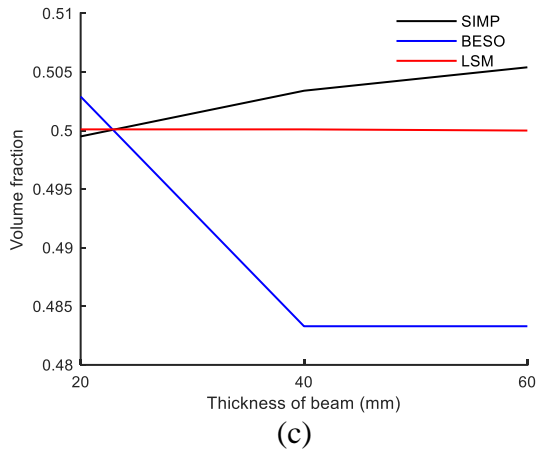


Figure 21 Results plot of section thickness: (a) compliance (kNm), (b) displacement (mm), (c) volume fraction, (d) number of iterations of SIMP, BESO and LSM models

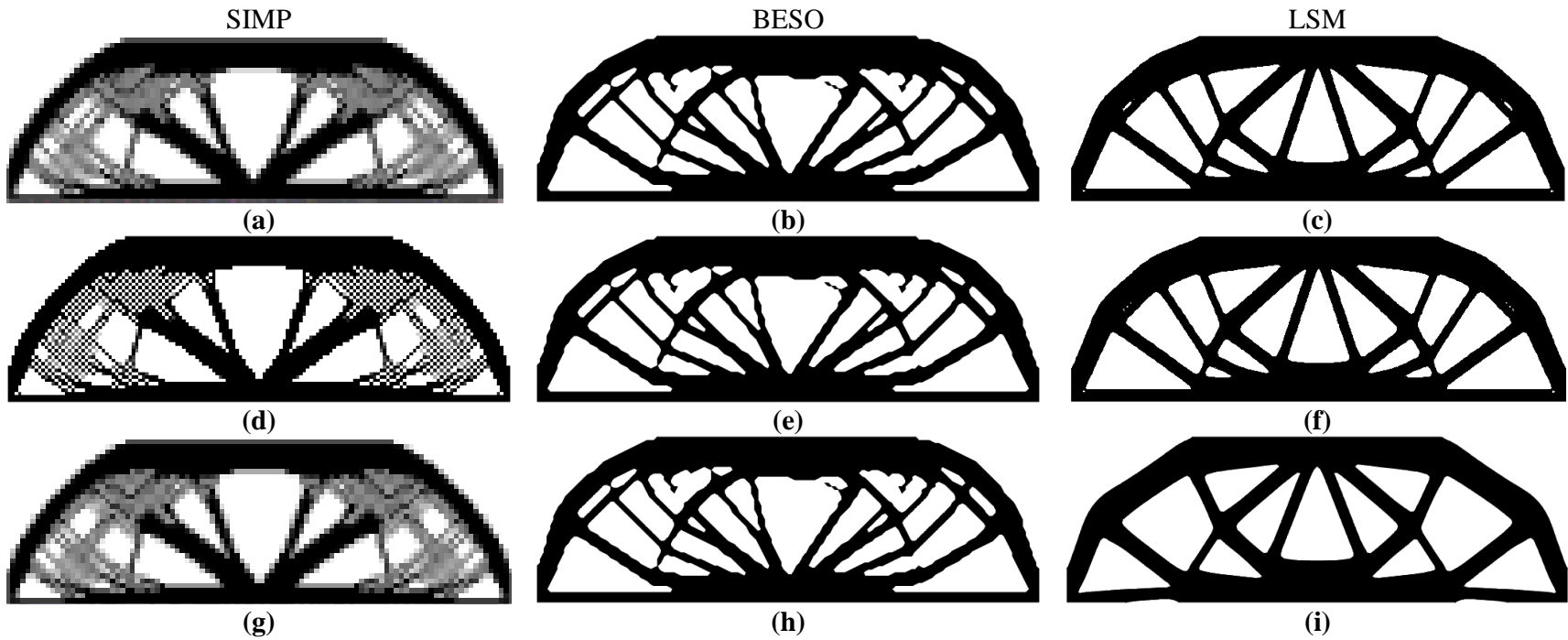


Figure 22 Topology optimized beams with different thicknesses: (a), (b), and (c) are optimized beams with thickness of 20mm for SIMP, BESO, and LSM, respectively. (d), (e), and (f) are optimized beams with thickness of 40mm for SIMP, BESO, and LSM, respectively. (g), (h), (i), are optimized beams with thickness of 60mm for SIMP, BESO, and LSM, respectively

5.3 Effect of Penalization Factor

Theoretically, a higher values of penalization factor leads to the elimination of intermediates densities and improves the stiffness of the material. Nevertheless, the results suggest that there is a threshold for the penalization factor (~ 3 to 4) to attain a well-optimized beam. On the other hand, the penalization factor had no significant effect on the structures optimized by LSM hence making it redundant as observed in all results illustrate in Figure 23

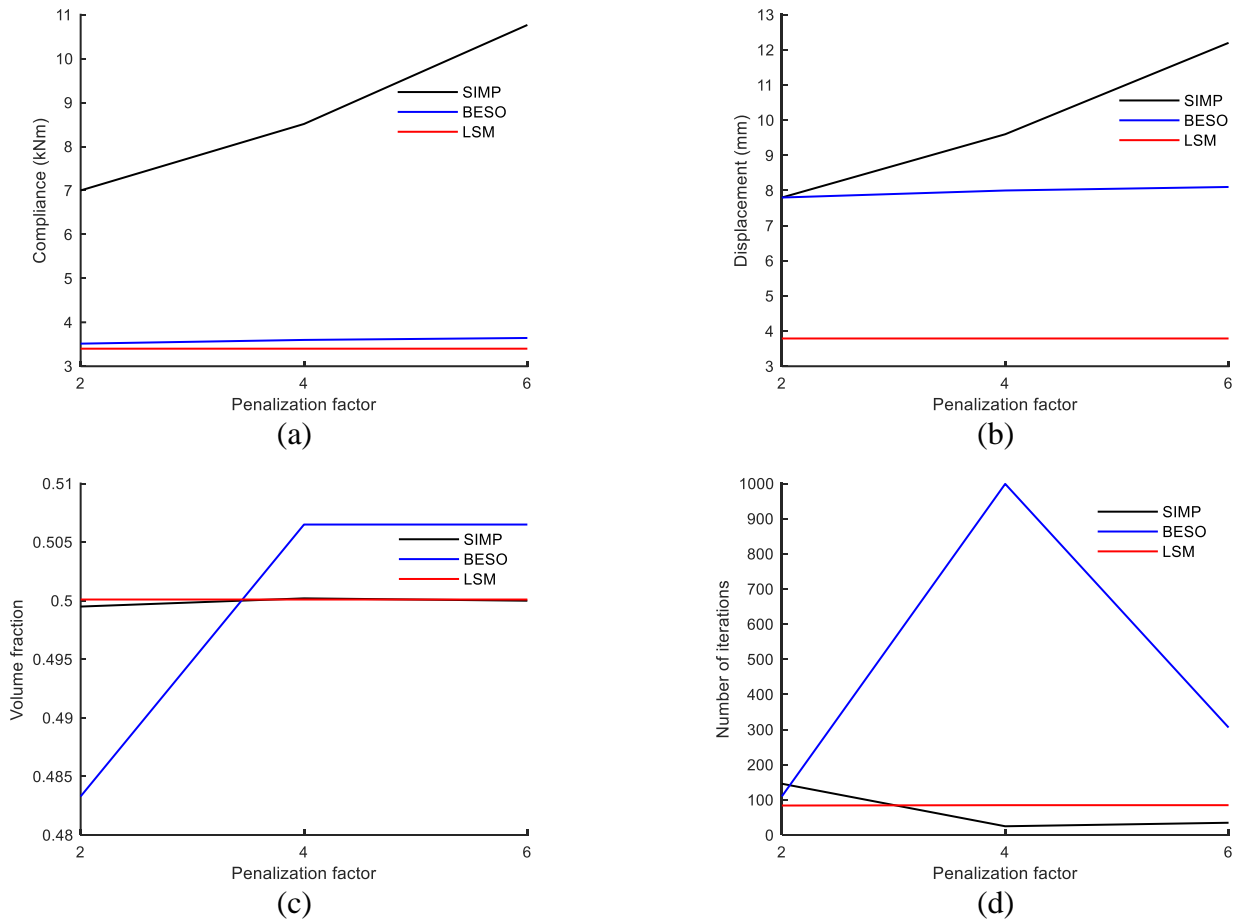


Figure 23 Results plot showing the effects penalization factor: (a) compliance (kNm), (b) displacement (mm), (c) volume fraction, and (d) number of iterations

In general, an increase in compliance and displacement is observed for structures optimized using SIMP and BESO, with an increase in the penalization factor. Also, as seen in Figure 24(d), the penalization factor resolves the checkerboard numerical instabilities. It was observed that the structures optimized using BESO did not have checkerboard numerical instabilities as shown in Figure 24. This can be attributed to the implementation of the bilinear interpolation scheme. However, caution should be taken in implementing these smoothing techniques as they are applied at the end of the optimization algorithm.

65

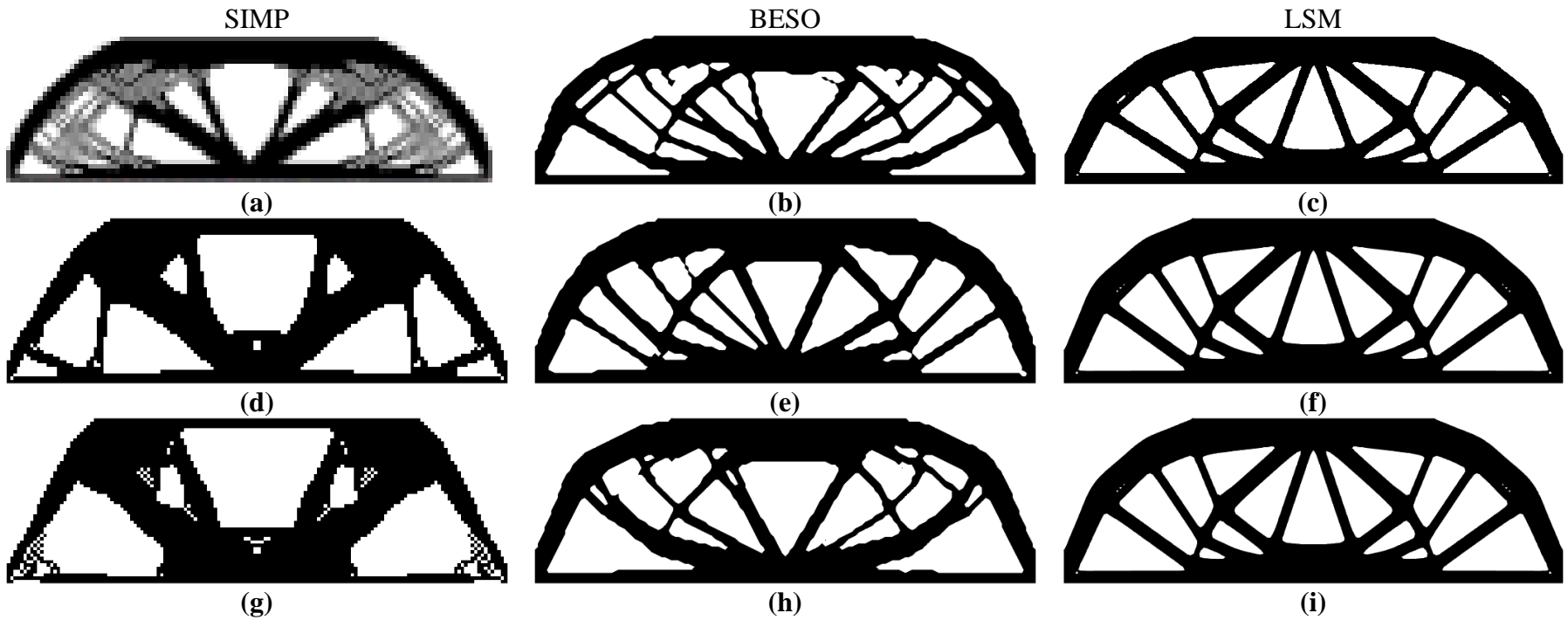


Figure 24 Effect of penalization factor on beams: (a), (b), and (c) are penalization factor of 2 for SIMP, BESO, and LSM, respectively. (d), (e), and (f) are penalization factor of 4 for SIMP, BESO, and LSM, respectively. (g), (h), and (i) are penalization factor of 6 for SIMP, BESO, and LSM, respectively.

5.4 *Effect of Desired Volume*

Ideally, a prescribed volume fraction of 0.5 might be the best solution due to the reduced mass of the structure. However, the overall optimal performance in terms of compliance and displacement should be considered before concluding. From Figure 25(a) and Figure 25(b), there is a gradual decrease in compliances and displacements. This implies better performance of beams with increasing density. The results suggests that a prescribed volume fraction of ranges 0.7 to 0.85 is optimal for structures optimized by any of the three optimization algorithms (i.e., SIMP, BESO, and LSM).

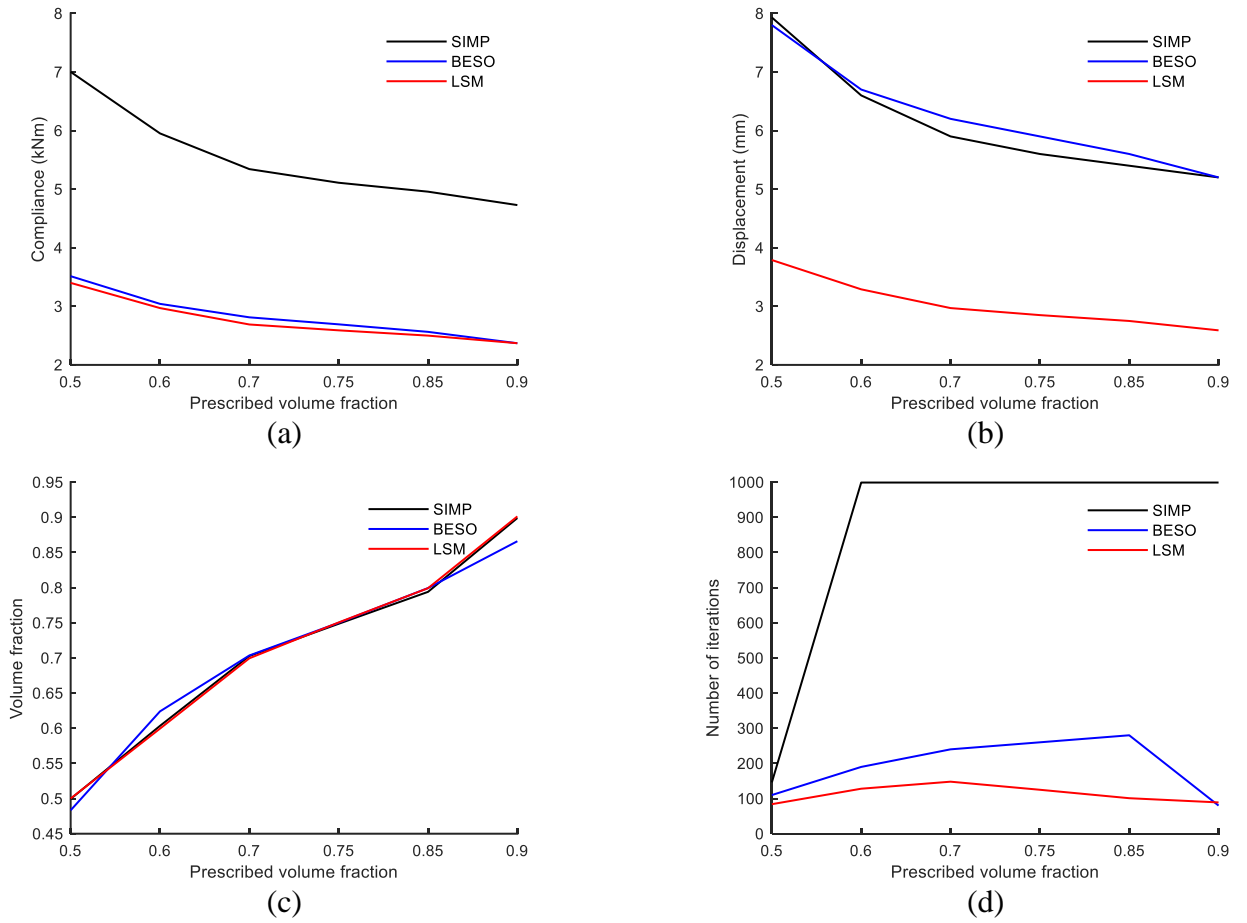


Figure 25 Effectiveness of prescribed volume fraction: (a) compliance (kNm), (b) displacement (mm), (c) volume fraction, and (d) number of iterations

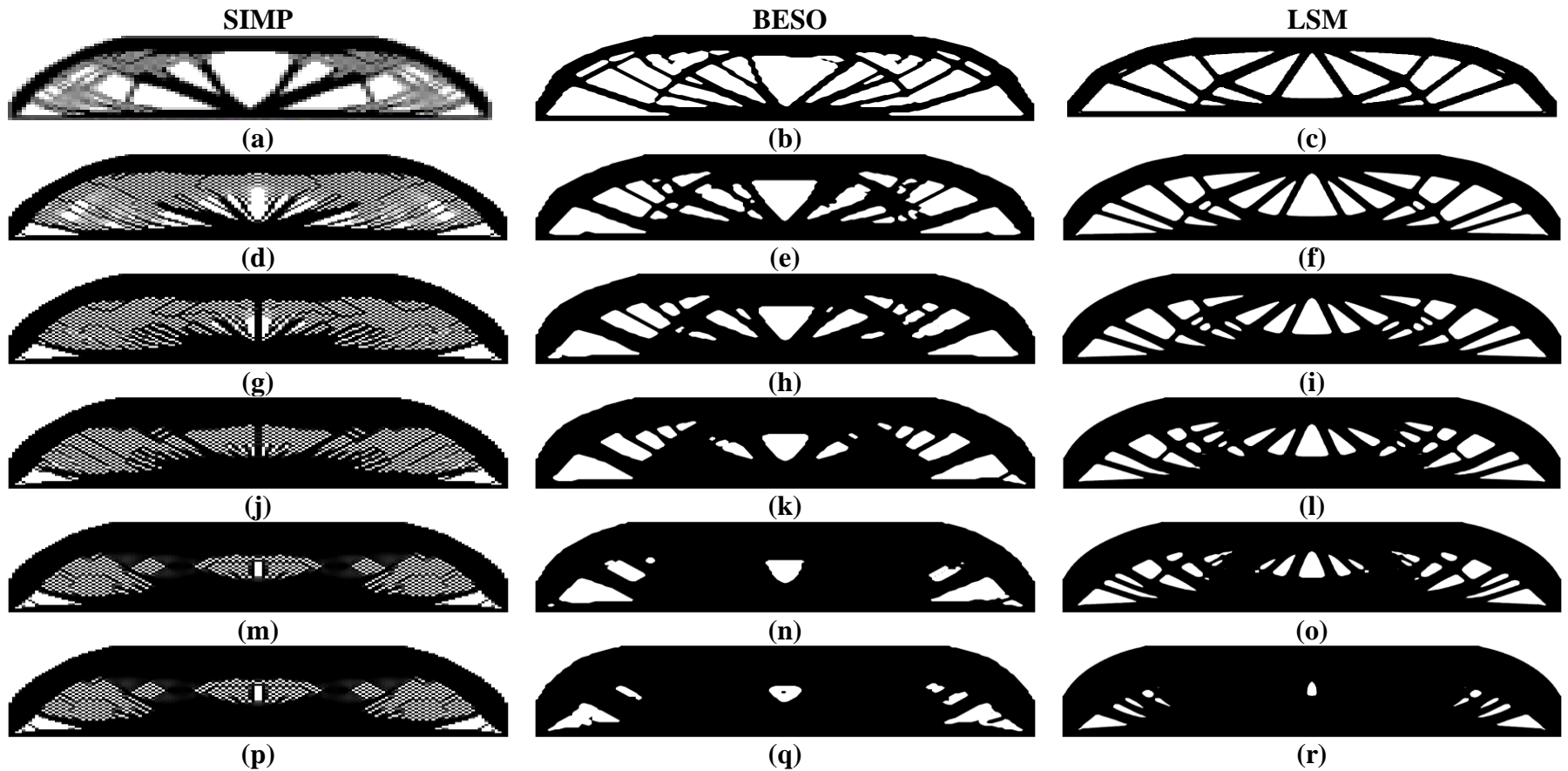


Figure 26 Optimized beams of different prescribed volume fractions: (a), (b), and (c) prescribed volume fraction of 0.5 for SIMP, BESO, and LSM, respectively. (d), (e), and (f) prescribed volume fraction of 0.6 for SIMP, BESO, and LSM, respectively. (g), (h), and (i) prescribed volume fraction of 0.7 for SIMP, BESO, and LSM, respectively. (j), (k), and (l) prescribed volume fraction of 0.75 for SIMP, BESO, and LSM, respectively. (m), (n), and (o) prescribed volume fraction of 0.8 for SIMP, BESO, and LSM, respectively. (p), (q) and (r) prescribed volume fraction of 0.9 for SIMP, BESO, and LSM, respectively

5.5 Effect of Filter Radius

Figure 27 illustrates the effect of applying mesh independent filters with varying filtering radius. The results indicated that for structures optimized using SIMP, a filter radius of 1 does not eliminate the checkerboard numerical instability. Furthermore, structures optimized by BESO with a filter radius of 1, did not result in applicable solutions as elements were disconnected abruptly. It should be noted that a bilinear interpolation scheme has been applied to structures optimized using BESO. This resolved the checkerboard numerical instabilities. Also, the results indicate that using a filter radius of 2 had developed gray areas (i.e., elements with intermediate densities), which is not an ideal case for manufacturing of the material. Therefore, a filter radius of 1.5 is recommended based on the results.

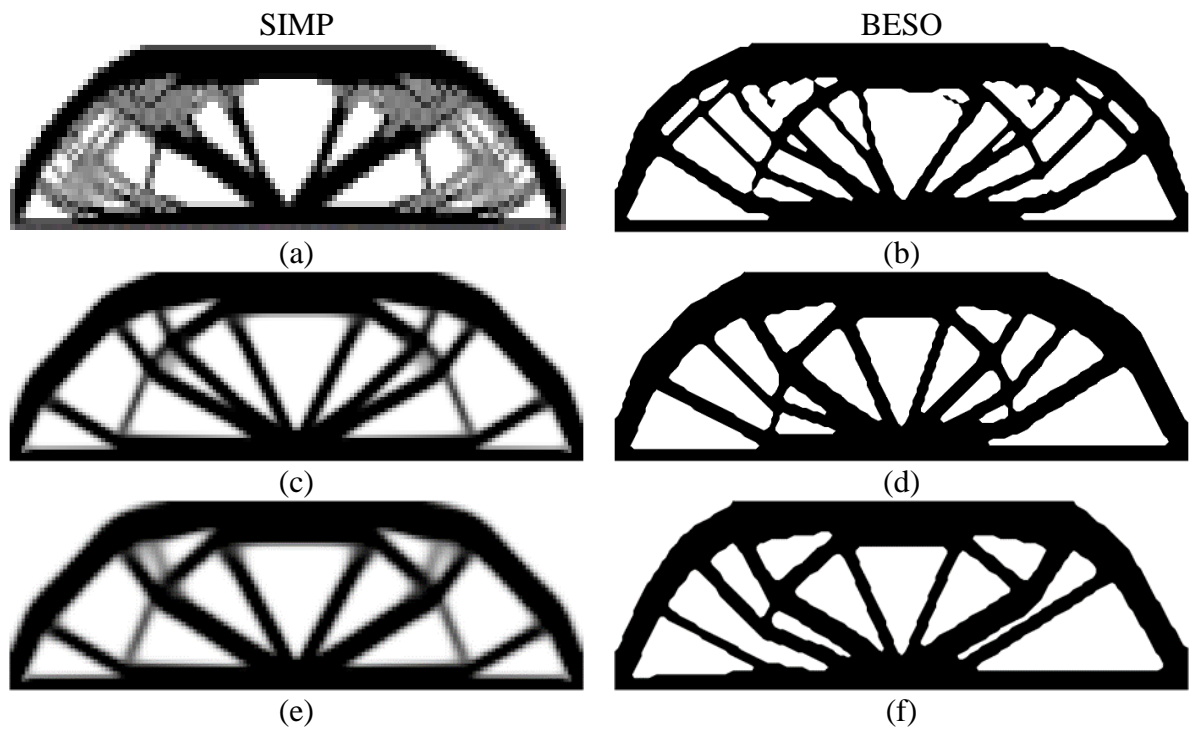
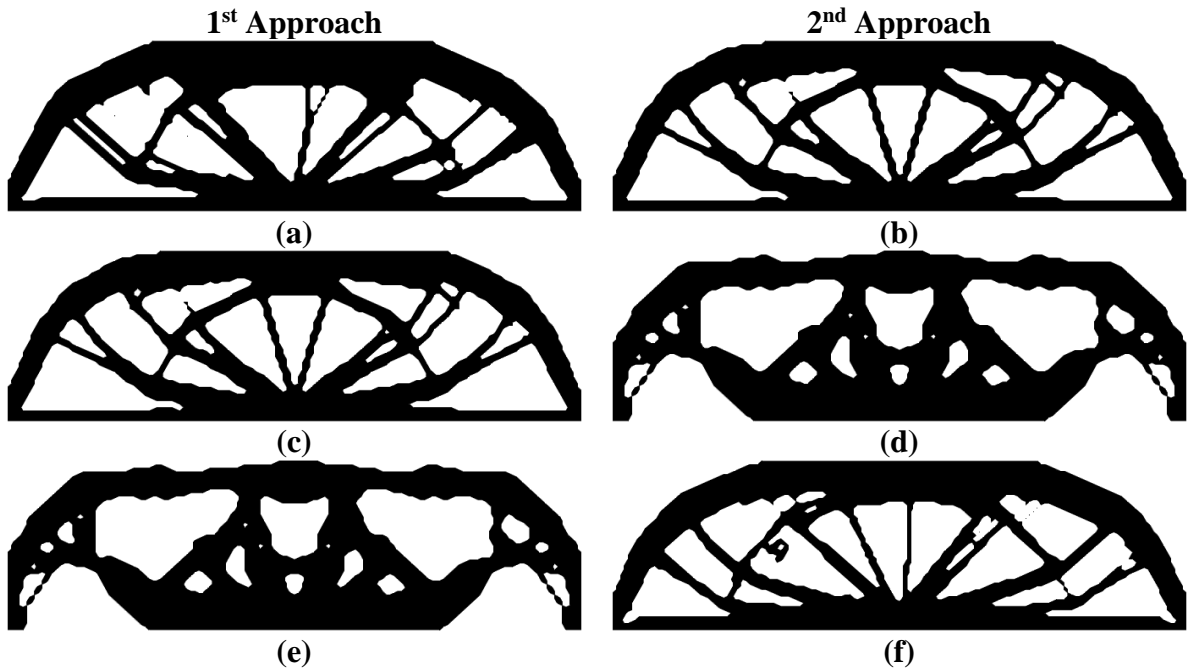


Figure 27 Effect of filter radius on topology optimized beams: (a) and (b) shows a filter radius of 1 for SIMP and BESO. (c) and (d) shows a filter radius of 1.5 for SIMP and BESO. (e) and (f) shows a filter radius of 2

5.6 Effect of Element Rejection Ratio and Addition Ratio

Figure 28 illustrates optimized structures with two approaches. The first approach had the structure optimized with equal element rejection ratio (ERR) and the maximum addition ratio (AR_{max}). In the second approach the structures were optimized with ERR to be different than the AR_{max} . It was observed that structures optimized using an ERR that is greater than AR_{max} led to unstable and distorted structures as seen in figure 28(e). A 5% removal and addition ratio of materials achieved an optimal solution in terms of density, compliance, displacement, and computational time. For structures optimized using the second approach, the recommended values for ERR and AR_{max} are 5% and 2%, respectively.



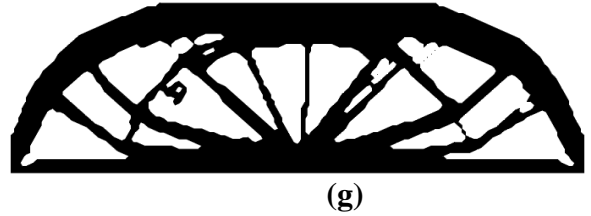


Figure 28. Effect of removal and additional ratio on BESO optimized beams: (a) ER and ARmax 0.01, (b) ER 0.05 and ARmax 0.02, (c) ER and ARmax 0.05, (d) ER 0.1 and ARmax 0.02, (e) ER and ARmax 0.10, (f) ER 0.02 and ARmax 0.05, and (g) ER 0.02 and ARmax 0.10.

5.7 Effect of Convergence Criteria

Figure 29 illustrates the final solution for structures optimized by BESO using various convergence criteria. The results suggest a minimal impact of the convergence criteria on the final solution. This is true when the convergence criteria are relatively small (i.e., <0.001).

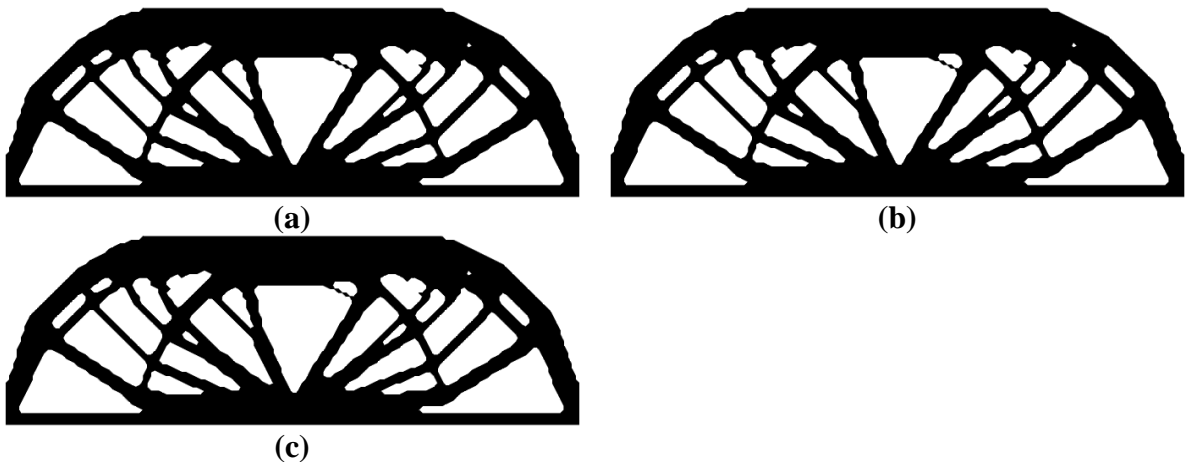


Figure 29. Convergence limit check of topology optimized beams: (a) convergence criteria of 0.001, (b) convergence criteria of 0.0001, and (c) convergence criteria of 0.00001

5.8 *Effect of Radius of Nucleated Holes*

Figure 30 illustrates the final solution for structures optimized by LSM using various radius of nucleated holes. The results suggest that using a large radius (i.e., greater than 20%) ratio would lead to a non-optimized structure. It is recommended to use a radius of 0.2 as it generates an optimal solution that can be easily manufactured.

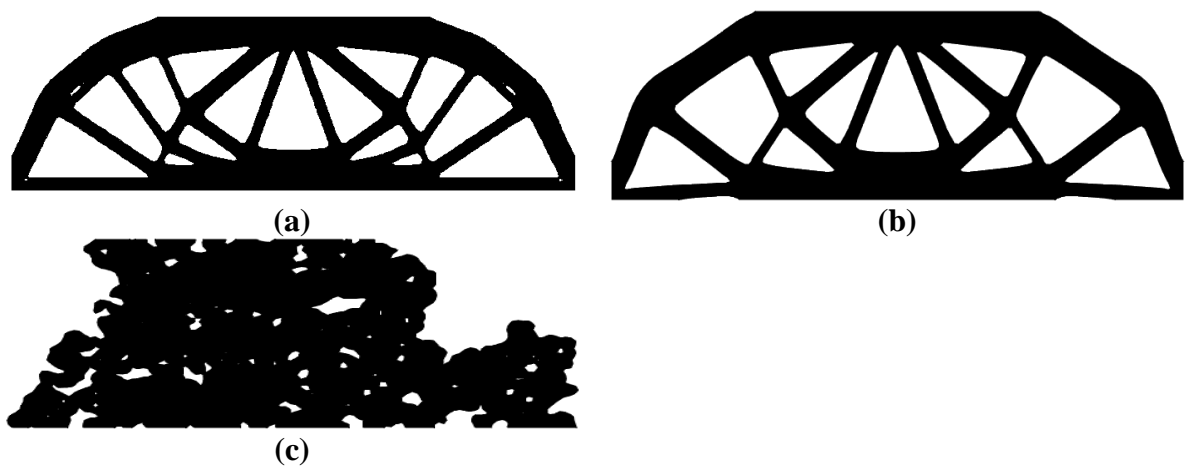


Figure 30. Radius of nucleated holes: (a) 10% of No. of y-elements, (b) 20% of No. of y-elements, and (c) 50% of No. of y-elements

5.9 *Preferred Parameters in Optimization of Beams*

In this section, the three topology optimization methodologies were implemented with the optimal values for the optimization parameters. The parameters used for the optimization in this section are presented in Table 2. All models were set to have a maximum number of iterations of 300.

Table 2. Preferred parameters for simulation

Element (x)	200
Element (y)	100
Thickness (mm)	60
Penalization factor (P)	4
Volume fraction	0.75
Filter radius	1.5
ERR	5%
AR_{\max}	2%
Radius of holes	20% of number of y -elements
Time step	0.5
Delta (Δ)	10
Weight control (μ)	20
γ	0.05

Represents parameters for SIMP, BESO, and LSM.
 Represents parameters for SIMP, and BESO only.
 Represents parameters for BESO only.
 Represents parameters for LSM only.

Figure 31(a) to Figure 31(c) illustrates the final solution for structures optimized using SIMP, BESO and LSM, respectively. A well-generated topology optimized layout was attained for all three models with SIMP and BESO having similar features.

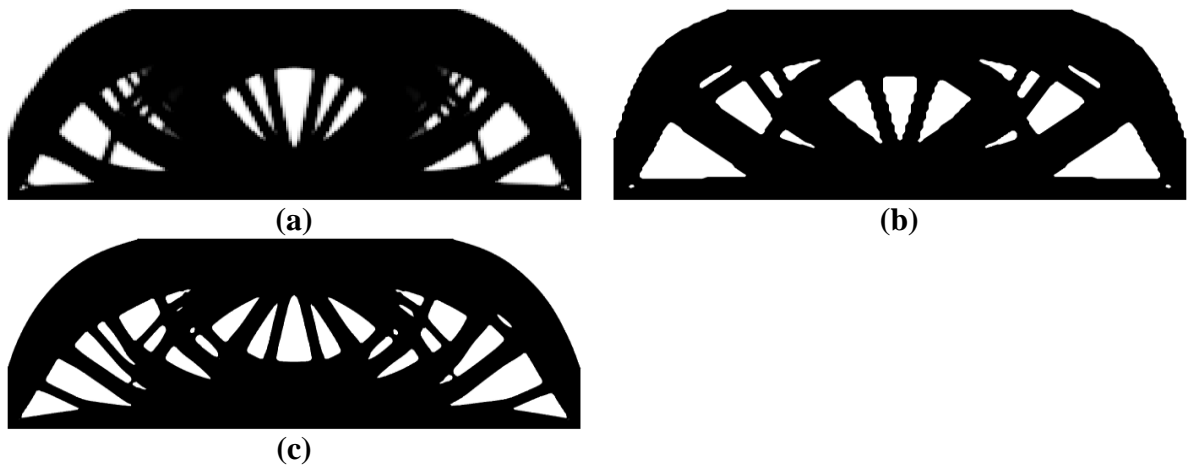
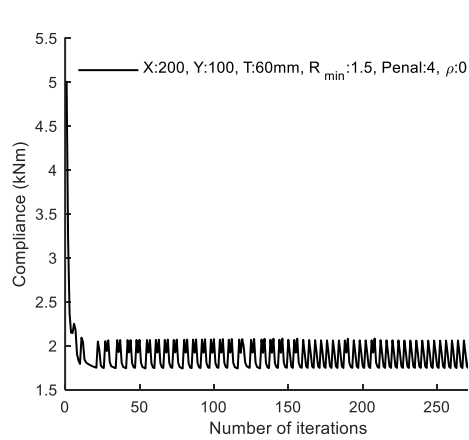
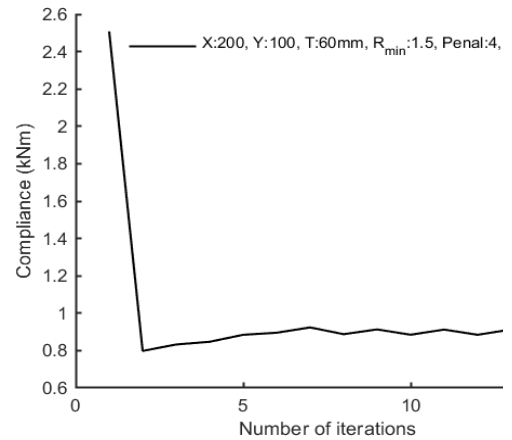


Figure 31. Optimized beams using preferred parameters: (a) SIMP, (b) BESO, and (c) LSM

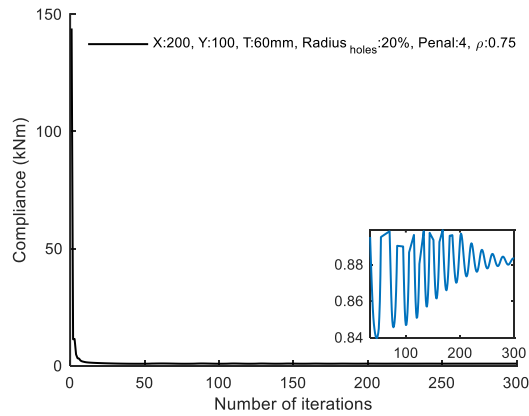
Figure 32(a) to Figure 32(c) display the compliance versus the number of iterations for structures optimized using SIMP, BESO and LSM, respectively. The compliance of SIMP was around 5kNm at the model initiation and reached 1.7661kNm at the 300th iteration. It should be noted that, the SIMP model was oscillating as seen in Figure 34(a). However, that did not affect the performance of the structure. The BESO model recorded a compliance of 2.5kNm at the initiation of the model and converged at the 15th iteration with a compliance of 0.9134kNm. In the case of structures optimized using LSM, it recorded a very high compliance at the model initiation. This is attributed to the nucleation of holes at the initial stage. However, the compliance reduced rapidly and reached 0.8833kNm at the 300th iteration.



(a)



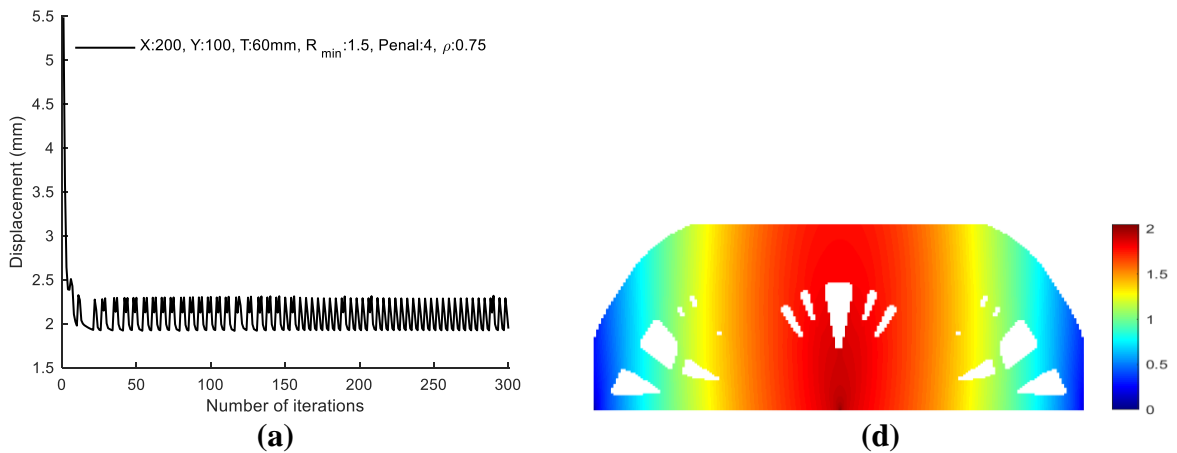
(b)



(c)

Figure 32. Compliance plot of beams with preferred parameters: (a) compliance of SIMP, (b) compliance of BESO, (c) compliance of LSM

Figure 33(d) to Figure 33(f) illustrate the displacement contour of the optimal solution by SIMP, BESO, and LSM, respectively. Table 3 presents a summary of the compliance and maximum displacement for the structures optimized using SIMP, BESO and LSM. The displacement of each model was analyzed with respect to the maximum displacement the conventional beam (i.e., completely solid) which was 1.14912mm (0.452in). The BESO model recorded the largest displacement of 2.0130mm (0.793in), with the SIMP model recording 1.9425mm (0.765in). The LSM model had a maximum displacement of 0.9715mm (0.382in), which outperformed the conventional model.



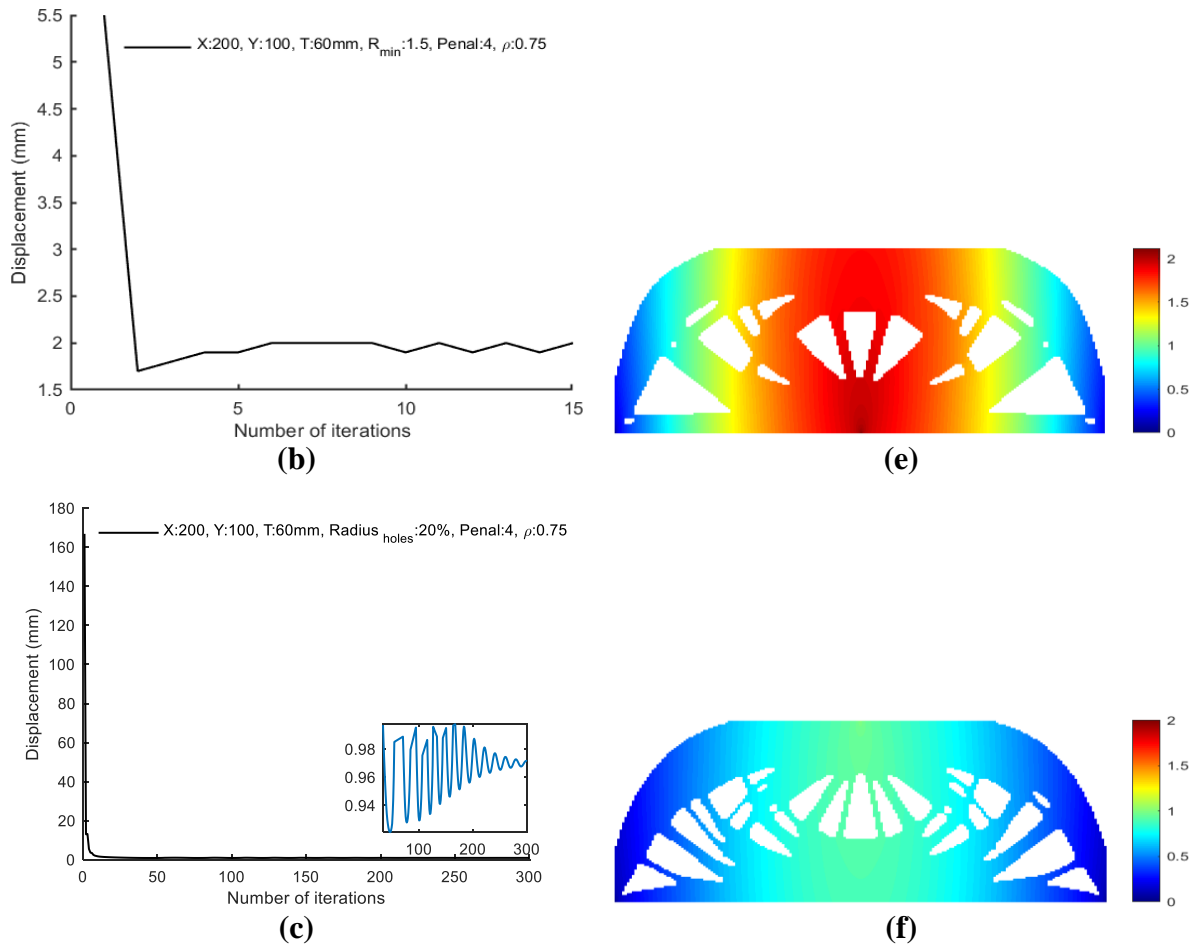


Figure 33. Displacement contour plot of optimized beams using preferred parameters: (a) displacement of SIMP, (b) displacement of BESO, (c) displacement of LSM, (d) displacement contour plot of SIMP, (e) displacement contour plot of BESO, (f) displacement contour plot of LSM

Table 3. Summary of Results from using Optimal Parameters for the Simulations

	Compliance (kNm)	Displacement (mm)	No of iterations
SIMP	1.7661	1.9425	300
BESO	0.9134	2.0130	15
LSM	0.8833	0.9715	300

Figure 34(a) to Figure 34(c) illustrate the variation in volume fraction with the number of iterations for structures optimized using SIMP, BESO and LSM. For the structure optimized by BESO, in the initial stages (i.e., in the first 5 iterations) elements are being removed. It is worth noting, that BESO might oscillate until it meets the convergence criteria after 15 iterations, only, as seen in Figure 34(b). In the LSM technique, initially holes are nucleated leading to a very small volume fraction as observed in Figure 34(c).

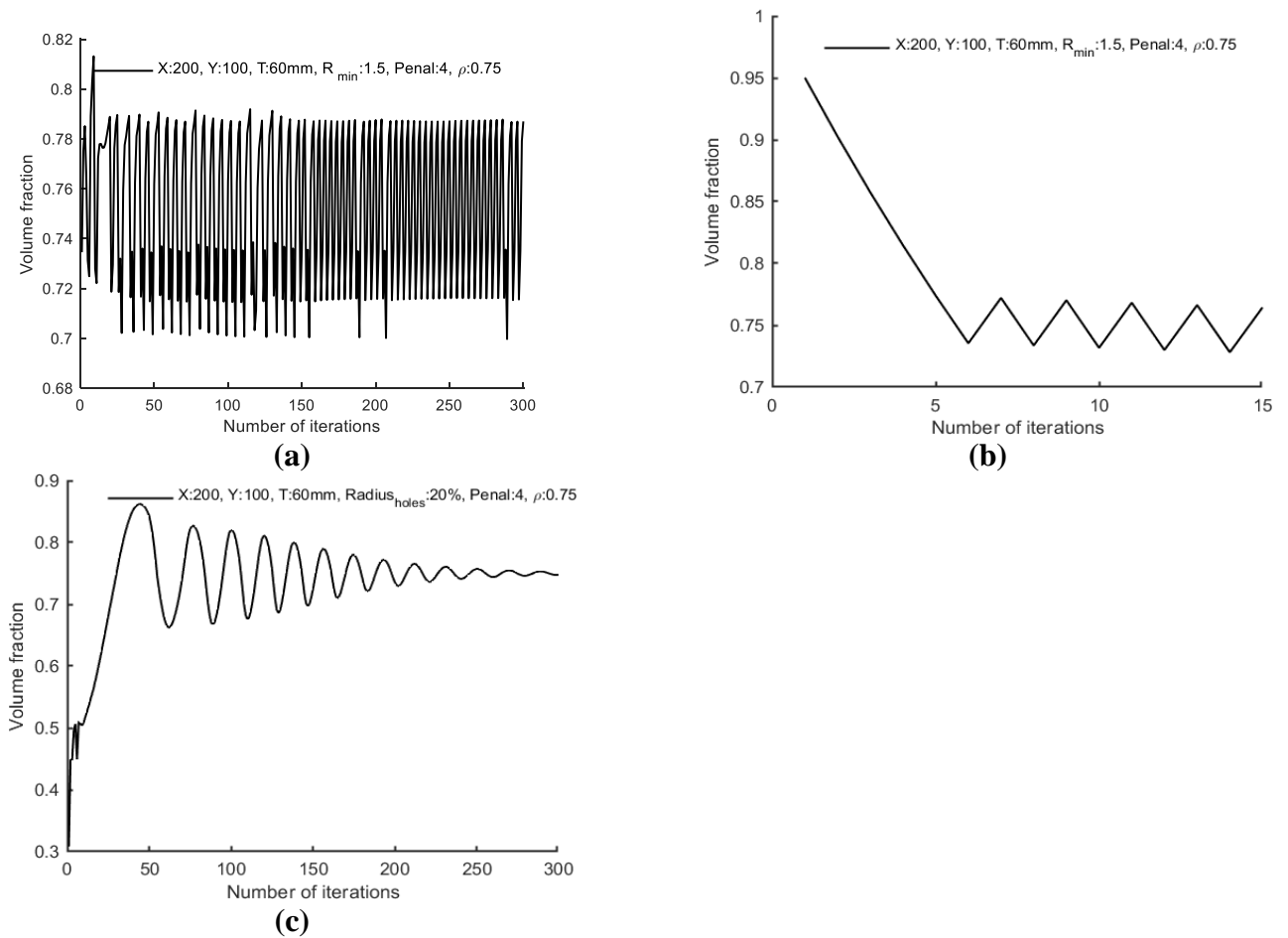


Figure 34. Volume Fraction Plot of Beams with Preferred Parameters Optimized with: (a) SIMP, (b) BESO, (c) LSM

CHAPTER 6

CONCLUSIONS AND RECOMMENDATIONS

In this thesis, the performance of three main compliance minimization optimization algorithms (SIMP, BESO and LSM) on optimizing a simply supported beam was analyzed. Initially, a review of the development and applications of topology optimization in the various fields was presented. It was followed by an explanation on the mathematical formulation and numerical implementation of the three topology optimization algorithms (SIMP, BESO and LSM). To identify the optimal range for the optimization parameters, several models were implemented and investigated with regards of the final optimal design, compliance and displacement performance.

In general, models with a dense mesh results in an accurate model more than models with a coarse mesh. For models optimized using SIMP and BESO, a filter radius of 1.5 results in a well-optimized structure and resolves numerical instabilities such as the checkerboard. Also, a penalization factor of 4 assist in minimizing the occurrence of the checkerboard numerical instabilities that might occur in models optimized by SIMP and BESO. A high penalization factor removed elements with intermediate densities and improved the stiffness of the structure. Additionally, utilizing a bilinear interpolation scheme as implemented in models optimized using BESO can eliminate elements with intermediate densities. However, precautions should be taken as it is a post-processing application.

Although mass minimization is a constraint as a light-weighted beam is sought, the smallest volume fraction is not the ideal volume fraction. The results indicated that models with a volume fraction ranging from 70% to 75% was optimal, in regard to the mechanical performance of the beam. Models optimized using BESO require the ERR to be greater than AR_{max} . Models optimized using LSM, should have a radius of holes to be nucleated within the range of 10% to 20%.

LSM is an implicit boundary method which makes it unique compared to SIMP and BESO and performed excellently. Despite this, there are certain challenges which can make the LSM difficult to implement. One of these has to do with the period of creating holes within the domain and the time step required for updating the velocities. Importantly, this thesis considered compliance as its objective function and does not account for stress failure modes. It is necessary to include stress-constraint in future works of topology optimization [99-101].

LIST OF REFERENCES

- [1].Li, Y., Zhu, J. H., Zhang, W. H., & Wang, L. (2018). Structural topology optimization for directional deformation behavior design with the orthotropic artificial weak element method. *Structural and Multidisciplinary Optimization*, 57(3), 1251-1266.
- [2].Eschenauer, H. A., & Olhoff, N. (2001). Topology optimization of continuum structures: a review. *Appl. Mech. Rev.*, 54(4), 331-390.
- [3].Gebisa, A. W., & Lemu, H. G. (2017, December). A case study on topology optimized design for additive manufacturing. In *IOP Conference Series: Materials Science and Engineering* (Vol. 276, No. 1, p. 012026). IOP Publishing.
- [4].Müller, T. E., & Klashorst, E. (2017). A quantitative comparison between size, shape, topology and simultaneous optimization for truss structures. *Latin American Journal of Solids and Structures*, 14(12), 2221-2242.
- [5].Byun, J. K., Park, I. H., Nah, W., Lee, J. H., & Kang, J. (2004). Comparison of shape and topology optimization methods for HTS solenoid design. *IEEE transactions on applied superconductivity*, 14(2), 1842-1845.
- [6].Zhou, M., Pagaldipti, N., Thomas, H. L., & Shyy, Y. K. (2004). An integrated approach to topology, sizing, and shape optimization. *Structural and Multidisciplinary Optimization*, 26(5), 308-317.
- [7].Munk, D. J., Auld, D. J., Steven, G. P., & Vio, G. A. (2019). On the benefits of applying topology optimization to structural design of aircraft components. *Structural and Multidisciplinary Optimization*, 60(3), 1245-1266.
- [8].Michell, A. G. M. (1904). LVIII. The limits of economy of material in frame-structures. *The London, Edinburgh, and Dublin Philosophical Magazine and Journal of Science*, 8(47), 589-597.
- [9].Save, M., & Prager, W. (Eds.). (2013). *Structural optimization: volume 1: optimality criteria* (Vol. 34). Springer Science & Business Media.
- [10]. Bendsoe, M. P., & Kikuchi, N. (1988). Generating optimal topologies in structural design using a homogenization method. *Computer methods in applied mechanics and engineering*, 71(2), 197-224.
- [11]. Krog L, Tucker A, Rollema G. *Application of Topology, Sizing and Shape Optimization Methods to Optimal Design of Aircraft Components*, Bristol: Altair Engineering.
- [12]. Smarslik, M., Ahrens, M. A., & Mark, P. (2019). Toward holistic tension- or compression-biased structural designs using topology optimization. *Engineering Structures*, 199, 109632.
- [13]. Bendsoe, M. P., & Sigmund, O. (2013). *Topology optimization: theory, methods, and applications*. Springer Science & Business Media.

- [14]. Ohsaki, M., & Swan, C. C. (2002). Topology and geometry optimization of trusses and frames. *Recent advances in optimal structural design*, 5, 97-123.
- [15]. Amir, O., & Sigmund, O. (2013). Reinforcement layout design for concrete structures based on continuum damage and truss topology optimization. *Structural and Multidisciplinary Optimization*, 47(2), 157-174.
- [16]. Amir, O., & Shakour, E. (2018). Simultaneous shape and topology optimization of prestressed concrete beams. *Structural and Multidisciplinary Optimization*, 57(5), 1831-1843.
- [17]. Zhou, L. Y., He, Z. Q., & Liu, Z. (2016). Investigation of optimal layout of ties in STM developed by topology optimization. *Structural Concrete*, 17(2), 175-182.
- [18]. Gaynor, A. T., Guest, J. K., & Moen, C. D. (2013). Reinforced concrete force visualization and design using bilinear truss-continuum topology optimization. *Journal of Structural Engineering*, 139(4), 607-618.
- [19]. Shakya, A., Nanakorn, P., & Petprakob, W. (2018). A ground-structure-based representation with an element-removal algorithm for truss topology optimization. *Structural and Multidisciplinary Optimization*, 58(2), 657-675.
- [20]. Smarslik, M., Ahrens, M. A., & Mark, P. (2019). Toward holistic tension-or compression-biased structural designs using topology optimization. *Engineering Structures*, 199, 109632.
- [21]. Gaynor, A. T., Guest, J. K., & Moen, C. D. (2013). Reinforced concrete force visualization and design using bilinear truss-continuum topology optimization. *Journal of Structural Engineering*, 139(4), 607-618.
- [22]. Yang, Y., Moen, C. D., & Guest, J. K. (2015). Three-dimensional force flow paths and reinforcement design in concrete via stress-dependent truss-continuum topology optimization. *Journal of Engineering Mechanics*, 141(1), 04014106.
- [23]. Wang, M. Y., & Zhou, S. (2004). Phase field: a variational method for structural topology optimization. *CMES-Computer Modeling in Engineering and Sciences*, 6(6), 547.
- [24]. Sokolowski, J., & Zochowski, A. (1999). On the topological derivative in shape optimization. *SIAM journal on control and optimization*, 37(4), 1251-1272.
- [25]. Wu, C. Y., & Tseng, K. Y. (2010). Topology optimization of structures using modified binary differential evolution. *Structural and Multidisciplinary Optimization*, 42(6), 939-953.
- [26]. Andreassen, E., Clausen, A., Schevenels, M., Lazarov, B. S., & Sigmund, O. (2011). Efficient topology optimization in MATLAB using 88 lines of code. *Structural and Multidisciplinary Optimization*, 43(1), 1-16.
- [27]. Hare, W., Nutini, J., & Tesfamariam, S. (2013). A survey of non-gradient optimization methods in structural engineering. *Advances in Engineering Software*, 59, 19-28.
- [28]. Carstensen, J. V., & Guest, J. K. (2018). Projection-based two-phase minimum and maximum length scale control in topology optimization. *Structural and Multidisciplinary Optimization*, 58(5), 1845-1860.
- [29]. Zhou, M., Lazarov, B. S., Wang, F., & Sigmund, O. (2015). Minimum length scale in topology optimization by geometric constraints. *Computer Methods in Applied Mechanics and Engineering*, 293, 266-282.

- [30]. Li, L., & Khandelwal, K. (2015). Topology optimization of structures with length-scale effects using elasticity with microstructure theory. *Computers & Structures*, 157, 165-177.
- [31]. Gebisa AW, Lemu HG. A case study on topology optimized design for additive manufacturing. In IOP Conference Series: Materials Science and Engineering 2017 Dec 1 (Vol. 276, No. 1, p. 012026). IOP Publishing.
- [32]. Zhu, J. H., Zhang, W. H., & Xia, L. (2016). Topology optimization in aircraft and aerospace structures design. *Archives of Computational Methods in Engineering*, 23(4), 595-622.
- [33]. Bakhtiary, N., Allinger, P., Friedrich, M., Mulfinger, F., Sauter, J., Müller, O., & Puchinger, M. (1996). A new approach for sizing, shape and topology optimization. *SAE transactions*, 745-761.
- [34]. Fredricson, H. (2005). Topology optimization of frame structures—joint penalty and material selection. *Structural and multidisciplinary optimization*, 30(3), 193-200.
- [35]. Fukushima, J., Suzuki, K., & Kikuchi, N. (1992). Shape and topology optimization of a car body with multiple loading conditions (No. 920777). SAE Technical Paper.
- [36]. Ge, D., Zhu, L., & Xuan, D. (2017). Topology Optimization in Electric Car Body Frame Based on Optistruct. In MATEC Web of Conferences (Vol. 100, p. 01016). EDP Sciences.
- [37]. Rousseau, J. (2004, February). Optimisation techniques leading the development of a steering wheel. In The Altair Technology Conference.
- [38]. Lee, D. C., Choi, H. S., & Han, C. S. (2006). Design of automotive body structure using multicriteria optimization. *Structural and Multidisciplinary Optimization*, 32(2), 161-167.
- [39]. Kim, S. I., Kang, S. W., Yi, Y.-S., Park, J., & Kim, Y. Y. (2018). Topology optimization of vehicle rear suspension mechanisms. *International Journal for Numerical Methods in Engineering*, 113(8), 1412–1433. <https://doi.org/10.1002/nme.5573>
- [40]. Park J, Sutradhar A, Shah JJ, Paulino GH. Design of complex bone internal structure using topology optimization with perimeter control. *Computers in biology and medicine*. 2018 Mar 1;94:74-84.
- [41]. Park, S. M., Park, S., Shin, S., Lee, H., Ahn, S. J., Kim, L., ... & Noh, G. (2020). Designing a mandibular advancement device with topology optimization for a partially edentulous patient. *The Journal of prosthetic dentistry*, 123(6), 850-859.
- [42]. Milazzo, M., Muyschondt, P. G., Carstensen, J., Dirckx, J. J., Danti, S., & Buehler, M. J. (2020). De novo topology optimization of total ossicular replacement prostheses. *Journal of the mechanical behavior of biomedical materials*, 103, 103541.
- [43]. Vilardell, A. M., Takezawa, A., Du Plessis, A., Takata, N., Krakhmalev, P., Kobashi, M., ... & Yadroitsev, I. (2019). Topology optimization and characterization of Ti6Al4V ELI cellular lattice structures by laser powder bed fusion for biomedical applications. *Materials Science and Engineering: A*, 766, 138330.

- [44]. Beghini, L. L., Beghini, A., Katz, N., Baker, W. F., & Paulino, G. H. (2014). Connecting architecture and engineering through structural topology optimization. *Engineering Structures*, 59, 716-726.
- [45]. Huang, X., & Xie, M. (2010). *Evolutionary topology optimization of continuum structures: methods and applications*. John Wiley & Sons.
- [46]. Jewett, J. L., & Carstensen, J. V. (2019). Topology-optimized design, construction and experimental evaluation of concrete beams. *Automation in Construction*, 102, 59-67.
- [47]. Gan, V. J., Wong, C. L., Tse, K. T., Cheng, J. C., Lo, I. M., & Chan, C. M. (2019). Parametric modelling and evolutionary optimization for cost-optimal and low-carbon design of high-rise reinforced concrete buildings. *Advanced Engineering Informatics*, 42, 100962.
- [48]. Zhu, B., Skouras, M., Chen, D., & Matusik, W. (2017). Two-scale topology optimization with microstructures. *ACM Transactions on Graphics (TOG)*, 36(4), 1.
- [49]. Allaire, G., Cavallina, L., Miyake, N., Oka, T., & Yachimura, T. (2019). The homogenization method for topology optimization of structures: old and new. *Interdisciplinary Information Sciences*, 25(2), 75-146.
- [50]. Sigmund, O. (1995). Tailoring materials with prescribed elastic properties. *Mechanics of Materials*, 20(4), 351-368.
- [51]. Lipton, R., & Stuebner, M. (2006). Inverse homogenization and design of microstructure for pointwise stress control. *The Quarterly Journal of Mechanics and Applied Mathematics*, 59(1), 139-161.
- [52]. Gao, J., Li, H., Luo, Z., Gao, L., & Li, P. (2020). Topology optimization of micro-structured materials featured with the specific mechanical properties. *International Journal of Computational Methods*, 17(03), 1850144.
- [53]. Yang, R., & Du, J. (2013). Microstructural topology optimization with respect to sound power radiation. *Structural and Multidisciplinary Optimization*, 47(2), 191-206.
- [54]. Yun, K. S., & Youn, S. K. (2018). Microstructural topology optimization of viscoelastic materials of damped structures subjected to dynamic loads. *International Journal of Solids and Structures*, 147, 67-79.
- [55]. Wang, M. Y., & Zhou, S. (2004). Phase field: a variational method for structural topology optimization. *CMES-Computer Modeling in Engineering and Sciences*, 6(6), 547.
- [56]. Sokolowski, J., & Zochowski, A. (1999). On the topological derivative in shape optimization. *SIAM journal on control and optimization*, 37(4), 1251-1272.
- [57]. Duysinx, P., & Sigmund, O. (1998, September). New developments in handling stress constraints in optimal material distribution. In *7th AIAA/USAF/NASA/ISSMO symposium on multidisciplinary analysis and optimization* (p. 4906).
- [58]. Cheng, G. D., & Guo, X. (1997). ϵ -relaxed approach in structural topology optimization. *Structural optimization*, 13(4), 258-266.
- [59]. Gebremedhen, H. S., Woldemicael, D. E., & Hashim, F. M. (2019). Three-dimensional stress-based topology optimization using SIMP method. *International Journal for Simulation and Multidisciplinary Design Optimization*, 10, A1.

- [60]. Suzuki, K., & Kikuchi, N. (1991). A homogenization method for shape and topology optimization. *Computer methods in applied mechanics and engineering*, 93(3), 291-318.
- [61]. Cazacu, R., & Grama, L. (2014). Overview of structural topology optimization methods for plane and solid structures. *Annals of the University of Oradea, Fascicle of Management and Technological Engineering*, 23(3), 1583-1591.
- [62]. Bendsøe, M. P., & Sigmund, O. (1999). Material interpolation schemes in topology optimization. *Archive of applied mechanics*, 69(9), 635-654.
- [63]. Bruns, T. E. (2005). A reevaluation of the SIMP method with filtering and an alternative formulation for solid-void topology optimization. *Structural and Multidisciplinary Optimization*, 30(6), 428-436.
- [64]. Chiandussi, G., Gaviglio, I., & Ibba, A. (2001). Topology optimisation with optimality criteria and a given volume Lagrange multiplier. In *Proceedings of the XXX National Conference of the Italian Association Stress Analysis* (pp. 1103-12).
- [65]. Fanni, M., Shabara, M. N., & Alkalla, M. G. (2020). A Comparison between Different Topology Optimization Methods.(Dept M (Production)). *Bulletin of the Faculty of Engineering. Mansoura University*, 38(4), 13-24.
- [66]. Shukla, A., & Misra, A. (2013). Review of optimality criterion approach scope, limitation and development in topology optimization. *International Journal of Advances in Engineering & Technology*, 6(4), 1886.
- [67]. Sigmund, O. (2001). A 99 line topology optimization code written in Matlab. *Structural and multidisciplinary optimization*, 21(2), 120-127.
- [68]. Svanberg, K. (1987). The method of moving asymptotes—a new method for structural optimization. *International journal for numerical methods in engineering*, 24(2), 359-373.
- [69]. Xie, Y. M., & Steven, G. P. (1992, December). Shape and layout optimization via an evolutionary procedure. In *Proceedings of the international conference on computational engineering science*.
- [70]. Chu, D. N., Xie, Y. M., Hira, A., & Steven, G. P. (1996). Evolutionary structural optimization for problems with stiffness constraints. *Finite elements in analysis and design*, 21(4), 239-251.
- [71]. Xie, Y. M., & Steven, G. P. (1993). A simple evolutionary procedure for structural optimization. *Computers & structures*, 49(5), 885-896.
- [72]. Papadrakakis, M., Tsompanakis, Y., Hinton, E., & Sienz, J. (1996). Advanced solution methods in topology optimization and shape sensitivity analysis. *Engineering computations*.
- [73]. Querin, O. M., Steven, G. P., & Xie, Y. M. (1998). Evolutionary structural optimisation (ESO) using a bidirectional algorithm. *Engineering computations*.
- [74]. Osher, S., & Sethian, J. A. (1988). Fronts propagating with curvature-dependent speed: Algorithms based on Hamilton-Jacobi formulations. *Journal of Computational Physics*, 79(1), 12-49
- [75]. Haber, R., & Bendsoe, M. (1998). Problem formulation, solution procedures and geometric modeling-Key issues in variable-topology optimization. *7th AIAA/USAF/NASA/ISSMO Symposium on Multidisciplinary Analysis and Optimization*, 4948

- [76]. Razvan, C. (2014). Overview of Structural Topology Optimization Methods for Plane and Solid Structures. *Annals of The Oradea University. Fascicle of Management and Technological Engineering.*, XXIII (XIII), 2014/3(3).
- [77]. van Dijk, N. P., Maute, K., Langelaar, M., & van Keulen, F. (2013). Level-set methods for structural topology optimization: A review. *Structural and Multidisciplinary Optimization*, 48(3), 437–4727
- [78]. Gibou, F., Fedkiw, R., & Osher, S. (2018). A review of level-set methods and some recent applications. *Journal of Computational Physics*, 353, 82–109.
- [79]. Liu, H., Tian, Y., Zong, H., Ma, Q., Wang, M. Y., & Zhang, L. (2019). Fully parallel level set method for large-scale structural topology optimization. *Computers & Structures*, 221, 13–27
- [80]. Mullen, P., McKenzie, A., Tong, Y., & Desbrun, M. (2007). A variational approach to Eulerian geometry processing. *ACM Transactions on Graphics*, 26(3), 66
- [81]. Fu, J., Xia, L., Gao, L., Xiao, M., & Li, H. (2019). Topology Optimization of Periodic Structures With Substructuring. *Journal of Mechanical Design*, 141(7), 071403
- [82]. Jiang, L., Chen, S., & Jiao, X. (2018). Parametric shape and topology optimization: A new level set approach based on cardinal basis functions. *International Journal for Numerical Methods in Engineering*, 114(1), 66–87
- [83]. Delgado, G., & Hamdaoui, M. (2019). Topology optimization of frequency dependent viscoelastic structures via a level-set method. *Applied Mathematics and Computation*, 347, 522–54117
- [84]. Chen, Q., Liu, J., Liang, X., & To, A. C. (2020). A level-set based continuous scanning path optimization method for reducing residual stress and deformation in metal additive manufacturing. *Computer Methods in Applied Mechanics and Engineering*, 29.
- [85]. Xing, X., Wang, M. Y., & Lui, B. F. Y. (2007). Parametric shape and topology optimization with moving knots radial basis functions and level set methods. *Min J (u, Φ)*, 1, 2.
- [86]. Gomes, A. A., & Suleman, A. (2006). Application of spectral level set methodology in topology optimization. *Structural and Multidisciplinary Optimization*, 31(6), 430–443.
- [87]. Fašková, Z., Čunderlík, R., & Mikula, K. (2010). Finite element method for solving geodesic boundary value problems. *Journal of Geodesy*, 84(2), 135–144.
- [88]. Using Radial Basis Functions for Surface Interpolation. (n.d.). Retrieved June 10, 2021, from COMSOL Multiphysics website: <https://www.comsol.com/blogs/using-radial-basis-functions-for-surface-interpolation/>
- [89]. Luo, J., Luo, Z., Chen, S., Tong, L., & Wang, M. Y. (2008). A new level set method for systematic design of hinge-free compliant mechanisms. *Computer Methods in Applied Mechanics and Engineering*, 198(2), 318–331.
- [90]. De Gournay, F. (2006). Velocity extension for the level-set method and multiple eigenvalues in shape optimization. *SIAM Journal on Control and Optimization*, 45(1), 343–367.

- [91]. Yamasaki, S., Nomura, T., Kawamoto, A., Sato, K., & Nishiwaki, S. (2011). A level set-based topology optimization method targeting metallic waveguide design problems. *International Journal for Numerical Methods in Engineering*, 87(9), 844–868
- [92]. Sigmund, O., & Petersson, J. (1998). Numerical instabilities in topology optimization: a survey on procedures dealing with checkerboards, mesh-dependencies and local minima. *Structural optimization*, 16(1), 68-75.
- [93]. Haber, R. B., Jog, C. S., & Bendsøe, M. P. (1996). A new approach to variable-topology shape design using a constraint on perimeter. *Structural optimization*, 11(1), 1-12.
- [94]. Lopes, B., Arruda, M. R. T., Almeida-Fernandes, L., Castro, L., Silvestre, N., & Correia, J. R. (2020). Assessment of mesh dependency in the numerical simulation of compact tension tests for orthotropic materials. *Composites Part C: Open Access*, 1, 100006.
- [95]. Song, J. H., & Kim, C. (2012). 3-D topology optimization based on nodal density of divided sub-elements for enhanced surface representation. *International Journal of Precision Engineering and Manufacturing*, 13(4), 557-563.
- [96]. Wei, P., Li, Z., Li, X., & Wang, M. Y. (2018). An 88-line MATLAB code for the parameterized level set method based topology optimization using radial basis functions. *Structural and Multidisciplinary Optimization*, 58(2), 831–849.
- [97]. Wang, S. Y., Lim, K. M., Khoo, B. C., & Wang, M. Y. (2007). An extended level set method for shape and topology optimization. *Journal of Computational Physics*, 221(1), 395–421.
- [98]. Morse, B. S., Yoo, T. S., Rheingans, P., Chen, D. T., & Subramanian, K. R. (2005). Interpolating implicit surfaces from scattered surface data using compactly supported radial basis functions. In *ACM SIGGRAPH 2005 Courses* (pp. 78-es)
- [99]. Duysinx, P., Van Miegroet, L., Lemaire, E., Brùls, O., & Bruyneel, M. (2008). Topology and generalized shape optimization: Why stress constraints are so important? *International Journal for Simulation and Multidisciplinary Design Optimization*, 2(4), 253–258.
- [100]. Hailu Shimels, G., Dereje Engida, W., & Fakhruldin Mohd, H. (2017). A comparative study on stress and compliance based structural topology optimization. *IOP Conference Series: Materials Science and Engineering*, 241, 012003.
- [101]. Zhou, Ming, & Fleury, R. (2016). Fail-safe topology optimization. *Structural and Multidisciplinary Optimization*, 54(5), 1225–1243.